The Astrophysical Journal, 339:126–148, 1989 April 1

FIELD K GIANTS IN GALACTIC HALO. II. IMPROVED ABUNDANCE AND KINEMATIC PARAMETERS

Kavan U. Ratnatunga
Dominion Astrophysical Observatory, Herzberg Institute for Astrophysics

and

K. C. Freeman
Mount Stromlo and Siding Spring Observatories, The Australian National University
Received 1988 May 26; accepted 1988 September 2

ABSTRACT

Our survey for distant *in situ* field K giants in the Galactic halo has been expanded to include more stars with intermediate abundances ([Fe/H] ≥ -0.7). We have developed an autocorrelation index which measures the integrated strength of many weak metal lines in slit spectra. This new index is shown to be a more reliable measure of abundance than the Ca II index used by Ratnatunga and Freeman in 1985. Our sample now appears to separate into two components with clearly different chemical and kinematical properties: (1) a metal-weak halo component, which is at most slowly rotating, and is seen out to about 15 kpc from the Galactic plane in our sample; and (2) a metal stronger thick disk component, which extends up to about 5 kpc from the plane, rotates with the disk, and has a line-of-sight velocity dispersion of about 50 km s^{-1}. These two components are in some respects similar to those found by Zinn for the Galactic globular clusters. The velocity dispersion of the metal-weak stars toward the SGP appears to be approximately constant at about 75 km s^{-1}, out to about 25 kpc from the Galactic plane. This is significantly less than the dispersion of about 122 km s^{-1} in the SA 127 field ($l = 272°$, $b = 38°$). The large-scale anisotropic velocity dispersion of the metal-weak halo has not yet been reconciled with its apparently near-spherical shape.

Subject headings: galaxies: internal motions — galaxies: The Galaxy — stars: late-type — stars: Population II — stars: stellar statistics

I. INTRODUCTION

Our aim is to locate and study a chemically and kinematically unbiased sample of field K giants out to about 25 kpc from the Sun. These giants are ideal probes of the structure and evolution of the outer parts of the Galaxy. The motivation for this survey is discussed in detail by Ratnatunga and Freeman (1985, hereafter RF1). In the long term, we plan to obtain complete samples of giants with absolute magnitudes brighter than $M_V = +1$. Such K giants have apparent magnitudes $13 < V < 18$ and colors $(B-V) > 0.7$. Stars in this color-apparent magnitude range were identified from automated photographic photometry of plates taken with the UK Schmidt telescope. Our initial survey covers the more limited apparent magnitude range $13 < V < 16$ and color range $(B-V)_{pg} > 0.9$. The giants were selected from among the numerous nearby disk dwarfs in this color–apparent magnitude range by the strength of the Mg*b* + MgH feature at 5100 Å (Ratnatunga and Freeman 1983) on objective prism spectra from the ESO 1 m Schmidt telescope. The dispersion was 450 Å mm^{-1} at Hγ and the spectra covered the wavelength range from the Schott GG475 filter cutoff at 4750 Å to the IIIa–J emulsion cutoff at 5380 Å. Digital spectra for this selection were obtained by image analysis of MSO PDS microdensitometer scans.

We surveyed three high galactic latitude fields each of 20 square degrees, designated by the Selected Areas which they include: SA 141 ($l = 240$, $b = -85$); SA 189 (277, -50), and SA 127 (272, +38). Slit spectra for about 100 of these giants were acquired, using the 4 m AAT and the MSO 1.88 m telescope, to measure line-of-sight velocities and metal abundances. The resolution of our spectra was 2 Å, and the typical *S/N* ratio was about 15. From these spectra it was straightforward to measure line-of-sight velocities (± 10 km s^{-1}) by standard correlation techniques: see RF1. The abundance measurements were unfortunately not so straightforward.

The Ca II H and K lines seen in even the most metal-weak giants appeared at first sight to be the best features for measuring the abundances of K giants. In RF1 we therefore used a Ca II index (e.g., Suntzeff 1980) which had been calibrated against abundance through observations of globular cluster giants and field stars covering the entire metal abundance range from solar to [Fe/H] = -4.5. This Ca II index is certainly suitable for measuring abundances of the more metal weak giants. However, it is known (e.g., Ratnatunga 1983) that the Ca II scale collapses for [Fe/H] $\gtrsim -1$. Because our initial aim was to study the most distant halo giants, the first stars chosen for slit spectroscopy (RF1) were those with almost featureless objective prism spectra. In RF1 we therefore used the Ca II index to estimate abundances, because we expected that most of our stars were metal-weak.

However, our subsequent development of an abundance index that works for metal-strong and metal-weak stars (see § II) showed that several of our giants are more metal-strong than the estimates in RF1. Because the photometric parallaxes for these giants depend on the adopted abundances (see RF1), the corresponding estimated distances are also in error. As a result, some of the dynamical conclusions of RF1 require revision.

In § II we describe a procedure to derive abundances from the large number of weak metal lines of an observed spectrum, without needing explicitly to define the continuum. This procedure appears to work well over the range $0 \gtrsim$ [Fe/H] $\gtrsim -2$.

Since preparing RF1, we have also acquired further spectroscopic and photoelectric data, and the full set of observations has now been reanalyzed.

In § III we discuss the procedures used for confirmation of luminosity class. In § IV we give a revised table of abundance, luminosity, distance, and line-of-sight velocity estimates for our K giants, and reanalyze the observed kinematics. In § V we discuss and summarize the current status of our study.

II. ABUNDANCE MEASUREMENT

Fourier cross-correlation techniques (for example, Tonry and Davis 1979) have become the standard for measuring line-of-sight velocities. We show that correlation techniques can also be used for a quantitative measure of the metal abundance of G and K giants that works over a wide range of abundances.

Briefly the procedure is as follows. We first select from the observed spectrum a wavelength interval with many weak metal lines. The Fourier transform of this section of the spectrum is then corrected for white noise and filtered to retain only the frequency range which is sensitive to the strength of the metal lines. The autocorrelation function is then evaluated from this filtered Fourier transform. The height of the autocorrelation peak is used as the abundance index and is calibrated by similar observations of giants of known abundance and color. For this calibration, we observe giants in globular clusters with known [Fe/H]. The calibration of the index against $(B-V)_0$ removes the net temperature dependence of the lines that contribute to the index. Since most of these are Fe lines,

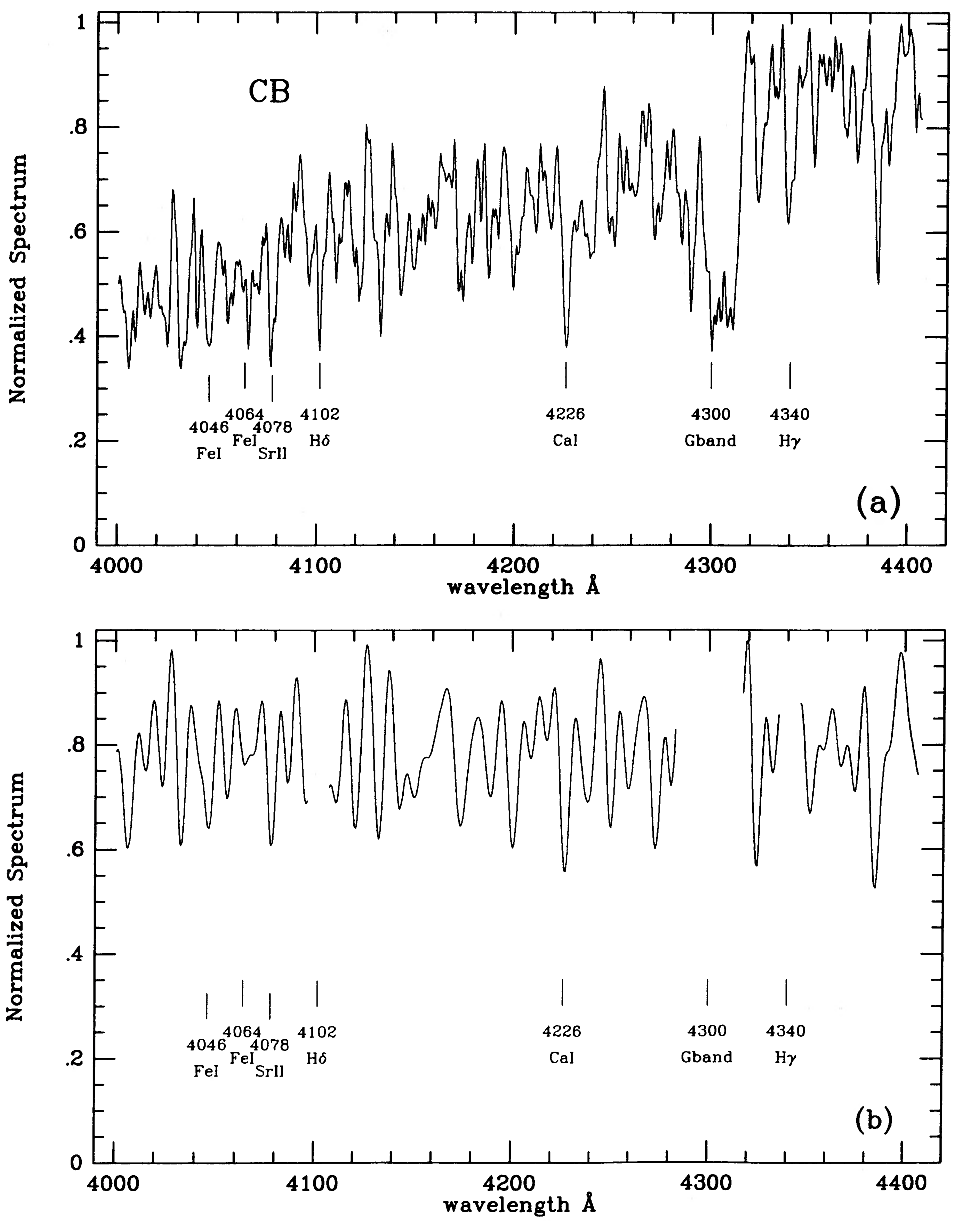

FIG. 1.—(*a*) The wavelength range of spectrum used to define the correlation index CB. Prominent spectral lines have been identified. (*b*) The spectrum after filtering shows the lines contributing to the index and the features of the spectra removed before evaluation of the index.

and as the index is calibrated against the [Fe/H] abundance of the globular clusters (from Zinn 1985), the index can be taken as a measure of the stellar [Fe/H].

Our slit spectra have been taken with three different telescope/detector/spectrograph combinations. Most of the spectra were taken with the AAT/IPCS/RGO spectrograph and covered the wavelength range 3650–5400 Å. We also have observations with the MSO 1.88 m telescope/blue 2D-photon counting array (B2PCA)/Cassegrain spectrograph, which covered only the blue wavelength range 3800–4450 Å, and some observations with the red 2D-photon counting array (R2PCA), which covered only the green region 4800–5400 Å. The resolution of the spectra for all these systems was 2 Å.

An autocorrelation index (CB) was defined on the wavelength range 4004–4411 Å. This region has a large number of metal lines, as illustrated on Figure 1*a*. Another index (CM) was defined on the wavelength range 4916–5343 Å and includes the Mg*b* triplet and a number of other strong Fe lines (Fig. 2*a*).

We now describe in detail the procedure used for the evaluation of abundance from the CB index. (A similar procedure was used for the CM index). The photon counts in the slit spectra had previously been wavelength-calibrated, sky-subtracted, and then SINC interpolated on to a log λ scale to measure line-of-sight velocities. First, we cut out the abundance-independent Balmer lines, namely Hδ at 4102 Å and Hγ at 4340 Å, since they would otherwise dominate the autocorrelation peak for the metal-weak stars. Excision of a 10 Å band for each Balmer line in the rest wavelength system was found to be sufficient. The G band (4283–4317 Å) was also cut out of the spectrum to ensure that this strong feature would not dominate the evaluated index. We do not interpolate

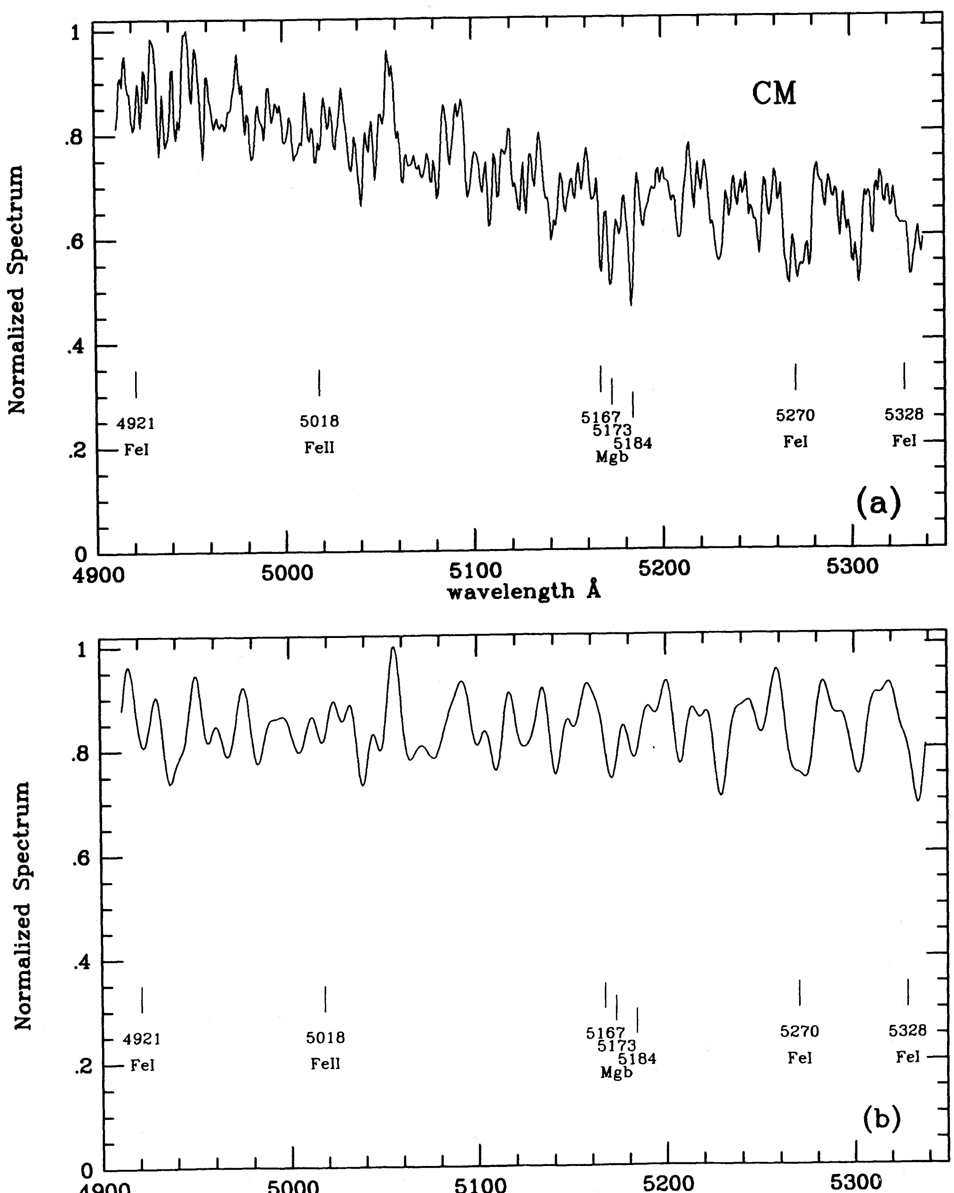

FIG. 2.—Same as Fig. 1 for the correlation index CM

across these features but just remove the pixels and close up the array; we note that the discontinuities across the cut-out regions are small compared to the photon noise.

The estimated contribution to the Fourier power spectrum from the photon noise (assumed to be white) is subtracted. In calculating the photon noise, the contribution to the noise from the sky background is also included. The autocorrelation function is then evaluated from the Fourier transform, after filtering out those frequencies which are insensitive to the strength of the metal lines, and is then normalized by the square of the mean photon counts in the spectrum. This procedure is necessary and sufficient to ensure that the index defined is independent of the signal to noise of the observation. We discuss below a Monte Carlo test used to check this independence.

Multiple observations of a metal-strong and a metal-weak local standard were used empirically to select the optimum frequency range in the power spectrum for abundance measurement. We choose this frequency range to maximize the ratio of abundance scale to measurement error. The low-frequency cutoff removes the instrumental response and low-frequency structure in the spectrum and contributes to minimizing the zero point correction between observations on different days. The high-frequency cutoff removes the noise dominated part of the power spectrum which would otherwise degrade the index.

Figure 3*a* compares the power spectra in the CB wavelength interval for the stars used to optimize the selected frequency range. The local standard Bok 45B is a [Fe/H] ≈ -1 halo giant, while Bok 17B is probably a solar abundance disk dwarf. The power spectrum of the extremely metal weak giant CD $-38°245$ with [Fe/H] $= -4.5$ is also shown. For each of these stars we have many independent observations and the error bars show the rms spread. For 512 pixel spectra (Nyquist frequency = 256), the frequency range 8–48 was found to be optimum. This frequency range corresponds to line widths from about 4 to 25 Å. Comparison of the filtered spectra in Figures 1*b* and 2*b* with Figures 1*a* and 2*a* shows the features contributing to the CB and CM indices.

Figure 3*b* compares the filtered autocorrelation functions for the two local standards and for CD $-38°245$. Again, the error bars show the rms spread for many independent observations.

Figure 3*c* shows the corresponding plot for the CM autocorrelation peak. The abundance index is defined as the height of the filtered autocorrelation peak above zero. (This was found to be better, in terms of the ratio of abundance scale to measurement error, than a peak-to-peak index.) We use 2.5 $\log_{10}$ (height of peak) to put the index on a magnitude scale, and add a suitable zero-point to ensure that the index is positive.

Abundance indices which use line and continuum bands in the spectrum (e.g., Friel 1987) are statistically independent of the mean count level of the spectrum. This is not necessarily so for our method; our noise subtraction procedure in the Fourier domain depends on the mean count level, and the effectiveness of this procedure needs to be tested. To check that our index has no residual dependence on mean counts, we use Monte Carlo simulations. Poisson noise, corresponding to different mean counts, is added to a metal-weak and a metal-strong template spectrum, and the abundance index is evaluated according to our procedure. As expected, the rms error of the measurements is larger for the metal weak spectrum that for the metal strong spectrum. Figure 4 shows how the abundance index varies with the effective mean count level of the simulated spectra. The error bars correspond to the rms scatter from the simulations (50 simulations were done for each point on the graphs, so the uncertainty of the mean index is about 0.14 of the error bars). There is no significant dependence on mean counts, except for the possible small increase of CM at very low counts in the metal weak spectrum. This is unimportant for our purposes, because none of our spectra are in this low count regime.

The abundance indices are first evaluated for all available spectra of globular cluster giants measured with the AAT/IPCS system. These observations calibrate the dependence of the CB index on $(B-V)_0$ and metal abundance, which is shown in Figure 5*a*. Since we have only a limited number of calibrating giants, we assume that the calibration is linear in [Fe/H] and $(B-V)_0$ within our range of color and abundance: i.e.,

$$[\mathrm{Fe/H}] = C_0 + C_1(B-V)_0 + C_2(\mathrm{CB}) . \qquad (1)$$

Since the rms error of the residuals for the CB calibration is only 0.15 dex, we believe that the available observations and the simple relationship given in equation (1) provide an adequate calibration of the CB abundance scale. Our only reservation is that we were unable to acquire observations of stars in the most metal-weak globular clusters, so our abundance scale for stars with [Fe/H] $\lesssim -1.8$ may not be precisely correct. However, the location of the extreme metal weak star CD $-38°245$ in Figure 5*a* shows that the CB abundance scale is still useful for abundances well below [Fe/H] $= -1.8$.

To further illustrate the magnitude of the error in the CB abundance system we show in Figure 5*b* the abundance of each calibration star against $(\mathrm{CB})_{(B-V)=1.0}$ defined by

$$(\mathrm{CB})_{(B-V)=1.0} = \mathrm{CB} - \frac{C_1}{C_2}\,[(B-V)_0 - 1.0] \; ; \qquad (2)$$

$(\mathrm{CB})_{(B-V)=1.0}$ is the abundance index adjusted to a standard color $(B-V) = 1.0$. A Mg*b* index is also evaluated as an additional measure of metal abundance. This index is evaluated conventionally, using a line band (5160–5190 Å) and continuum bands on either side between (5050–5060 Å) and (5235–5250 Å). The residuals of the Mg*b* and the CM abundance calibrations, from a relationship of similar form to equation (1), are about 0.25 dex, so more stars are needed to constrain the calibration. We therefore include our program field giants, with their CB abundances, in the calibration of the Mg*b* and the CM abundance scale; thus the three abundance scales are not independent, although the measurements themselves are of course independent. Only giants with photoelectric photometry are used in this calibration. Figures 6*a* and 6*b* show the comparison of the abundances estimated from the Mg*b* index and CM with $[\mathrm{Fe/H}]_{\mathrm{CB}}$. The residuals in the sense $[\mathrm{Fe/H}]_{\mathrm{CM}} - [\mathrm{Fe/H}]_{\mathrm{CB}}$ etc. are shown against $(B-V)$ in Figures 6*c* and 6*d*. The rms errors of the Mg*b* and CM abundances are about 0.30 dex. CM is clearly not as good a measure of abundance as CB, since this region of the spectrum has fewer metal lines (cf. Figs. 1 and 2).

For the green spectra our abundance estimate is the mean from Mg*b* and CM. For the blue spectra we use CB. For the IPCS spectra, we can estimate an abundance from both the green and the blue, and we take the average of these two abundance estimates.

Each instrument/detector/spectrograph system should be calibrated independently. However, this is not possible for the

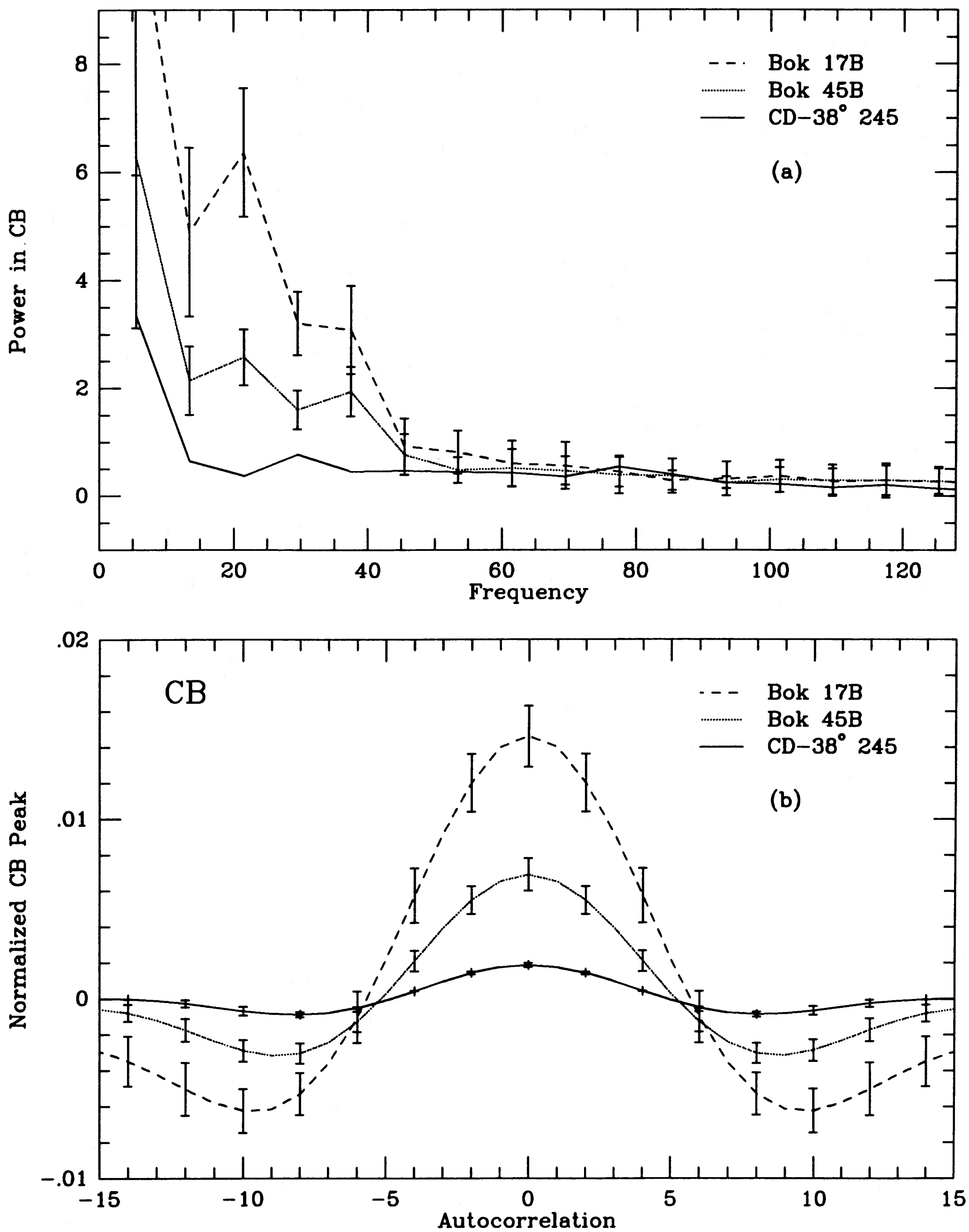

FIG. 3.—Fig. 3*a* compares smoothed power spectra of the stars used to optimize the frequency range for evaluating CB. The local standards Bok 45B and Bok 17B are a halo giant with [Fe/H] ≈ -1 and a probable solar abundance disk dwarf, respectively. CD $-38°245$ is the extremely metal weak giant with [Fe/H] $= -4.5$. Fig. 3*b* compares the CB autocorrelation peak from the filtered spectra. The observed rms scatter for multiple observations is shown by the error bars. Fig. 3*c* compares the CM autocorrelation peak from the filtered power spectra.

limited available MSO/PCA observations. Therefore, we derive a linear transformation from the MSO/PCA indices to the AAT/IPCS indices, using all stars observed in common with both systems, and then use the AAT/IPCS calibration of each index to derive an abundance from the MSO/PCA observations. To check the validity of this indirect procedure, we compare in Figure 7 the abundances of these stars estimated from observations with the MSO/PCA and the AAT/IPCS systems, using the CB, CM, and Mg*b* indices.

Local standards were observed regularly on each night and were used to remove any small residual systematic night-to-night differences in the abundance indices.

III. LUMINOSITY CLASSIFICATION

The MgH band at 5100 Å in the objective prism spectra removed most of the disk dwarfs from our catalog of stars with $(B-V)_{pg} > 0.9$. All of the stars being considered now have

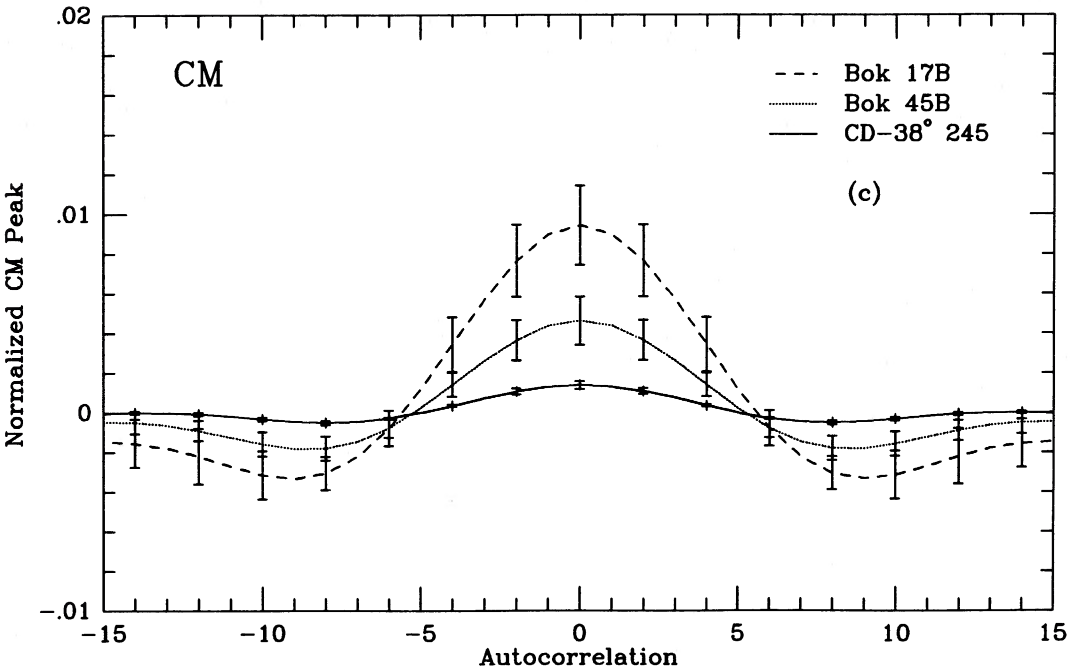

FIG. 3—*Continued*

objective prism spectra very similar to that of a giant, with undetectable MgH.

The photographic photometry used to select the giants for the survey has an estimated rms color error $\sigma_{pg} = 0.07$ mag. This is adequate for the selection of stars for objective prism measurement. However, photoelectric photometry is essential for the selected giant candidates, because the MgH feature is weak in G dwarfs with $(B-V) \lesssim 0.8$. Therefore dwarfs with a large negative photographic color error can be misidentified as candidate giants by our preliminary selection procedure. Since dwarfs comprise over 90% of the stars with $(B-V)_{pg} > 0.9$, the blue tail of the color error distribution beyond about 1.5 σ_{pg} will lead to significant dwarf contamination among the stars with measured $(B-V)_{pg} \approx 0.9$. The giant-like stars selected for further observation were classified into two groups from the appearance of their objective prism spectra: Group *a* had no visible features, these are mainly metal-weak giants if $(B-V)_{pe} \gtrsim 0.9$ but may include a few dwarfs with $(B-V)_{pe} \lesssim 0.8$, selected because of errors in the photographic photometry. Group *b* had no MgH band but a clear Mg*b* feature; these are either metal-strong giants or disk dwarfs with $(B-V)_{pe} \lesssim 0.9$.

We can estimate the expected dwarf contamination, using the observed color distribution and the estimated $\sigma_{pg} = 0.07$ mag for the photographic colors. If we select all stars redder than $(B-V)_{pg} = 0.9$, we expect about 2.5% of the sample to have $(B-V)_{pe} < 0.8$. As most of the stars are disk dwarfs, the dwarfs from this blue tail of the error distribution contaminate the sample in group *b* above. Group *b* stars are about 7% of the total with $(B-V)_{pg} > 0.9$, and we therefore expect that about one third of the group *b* stars are in fact hotter dwarfs. We note that group *b* stars with $(B-V)_{pg} > 1.1$ [which are safely 3 σ_{pg} above $(B-V)_{pg} \approx 0.9$], and all of the group *a* stars are not significantly affected by this contamination.

Another level of selection, using more accurate colors and slit spectroscopy, is therefore needed to weed out the remaining dwarfs. We were able to obtain photoelectric photometry for most of our stars. For some of the remainder, which were observed with the AAT/IPCS, we derived improved estimates of the $(B-V)$ color from the extinction corrected spectra, by constructing a broad band color index between ($\lambda\lambda$4000–4500 and $\lambda\lambda$4850–5350). This color index was transformed to the standard $(B-V)$ color by using stars with available photoelectric photometry that were observed spectroscopically on the same night. The effects of atmospheric refraction were minimized by keeping the spectrograph slit aligned along the parallactic angle throughout the observations. Figure 8*a* shows the spectrophotometrically derived $(B-V)$ colors against the available photoelectric values and includes data from all our nights. For uniformity, the separate observations of the six local standard stars have been averaged; each point represents an individual star. The rms scatter in the spectrophotometric color $(B-V)_{sp}$ is 0.05 mag. A few stars that had photoelectric colors and are now known to be contaminating dwarfs are represented by filled symbols.

Figure 8*b* shows the original *photographic* $(B-V)$ colors against their photoelectric or spectrophotometric colors, for all the stars which were selected for AAT/IPCS observation and have available photoelectric photometry. This figure shows clearly that some of these stars are in fact significantly bluer than their photographic colors. In particular, the stars that are now known to be contaminating dwarfs (represented by filled symbols) are systematically bluer, as we would expect from the discussion above.

For the stars with AAT/IPCS spectra, any residual dwarf contamination is removed from the selected candidates by comparing the strengths of the Sr II λ4078 and the Fe I λ4064 lines. In K giants the Sr II line is stronger, while in dwarfs of similar color the Fe I line is very much stronger (Morgan, Keenan, and Kellman 1943). This final check was done visually, using plots like those illustrated in Figures 9*a* and 9*c*.

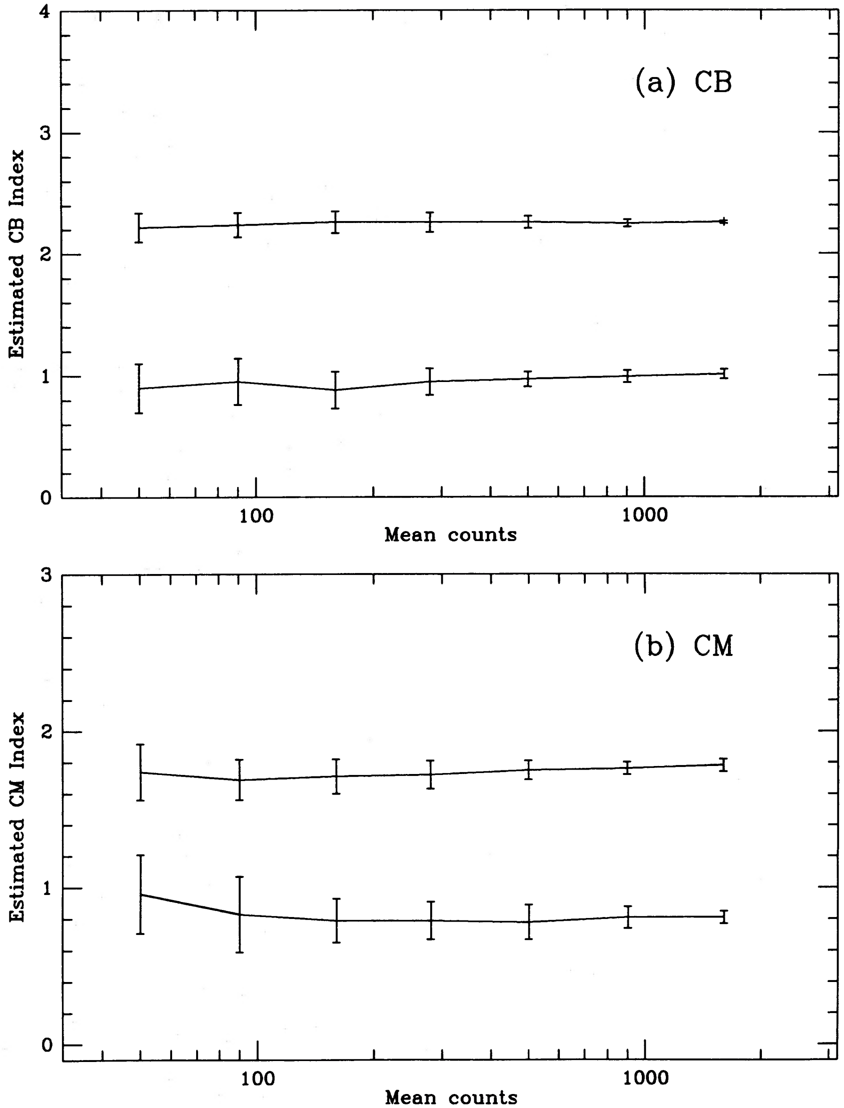

FIG. 4

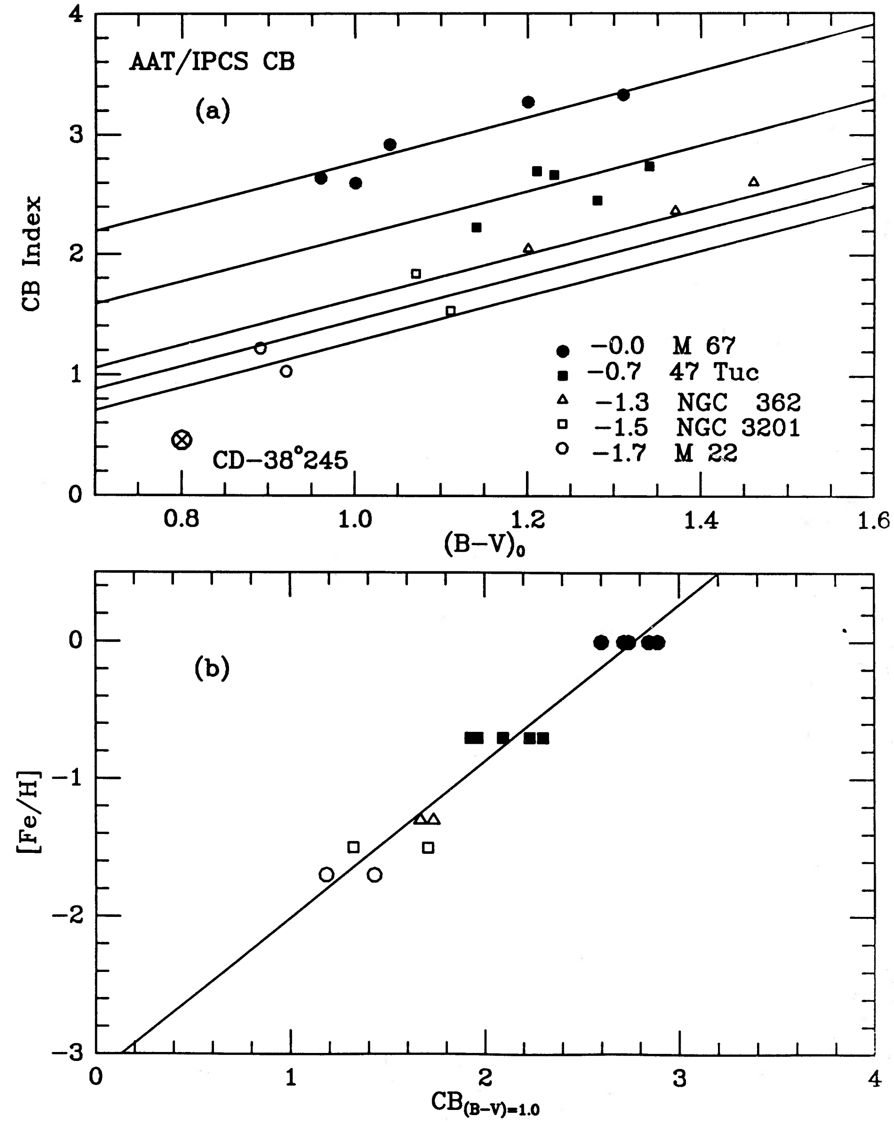

FIG. 5

FIG. 4.—Result of Monte Carlo simulations used to check the independence of the abundance indices to mean count level of the spectra. The appropriate Poisson noise is added to the spectra of a metal-weak (*lower line*) and metal-strong (*upper line*) template star in the evaluation of both indices CB and CM. The error bars show the rms scatter of the indices from this test, for 50 Monte Carlo simulations per point. The standard error of the mean index is 0.14 of the error bars.

FIG. 5.—(*a*) Dependence of the CB index on $(B-V)_0$ and metal abundance of cluster giants. Symbols for each cluster and the adopted metal abundance are shown. Data for the extremely metal weak giant CD $-38°245$ are also shown. (*b*) Dependence of [Fe/H] on $\mathrm{CB}_{(B-V)=1.0}$. The rms error of the abundance fit to eq. (1) is 0.15 dex.

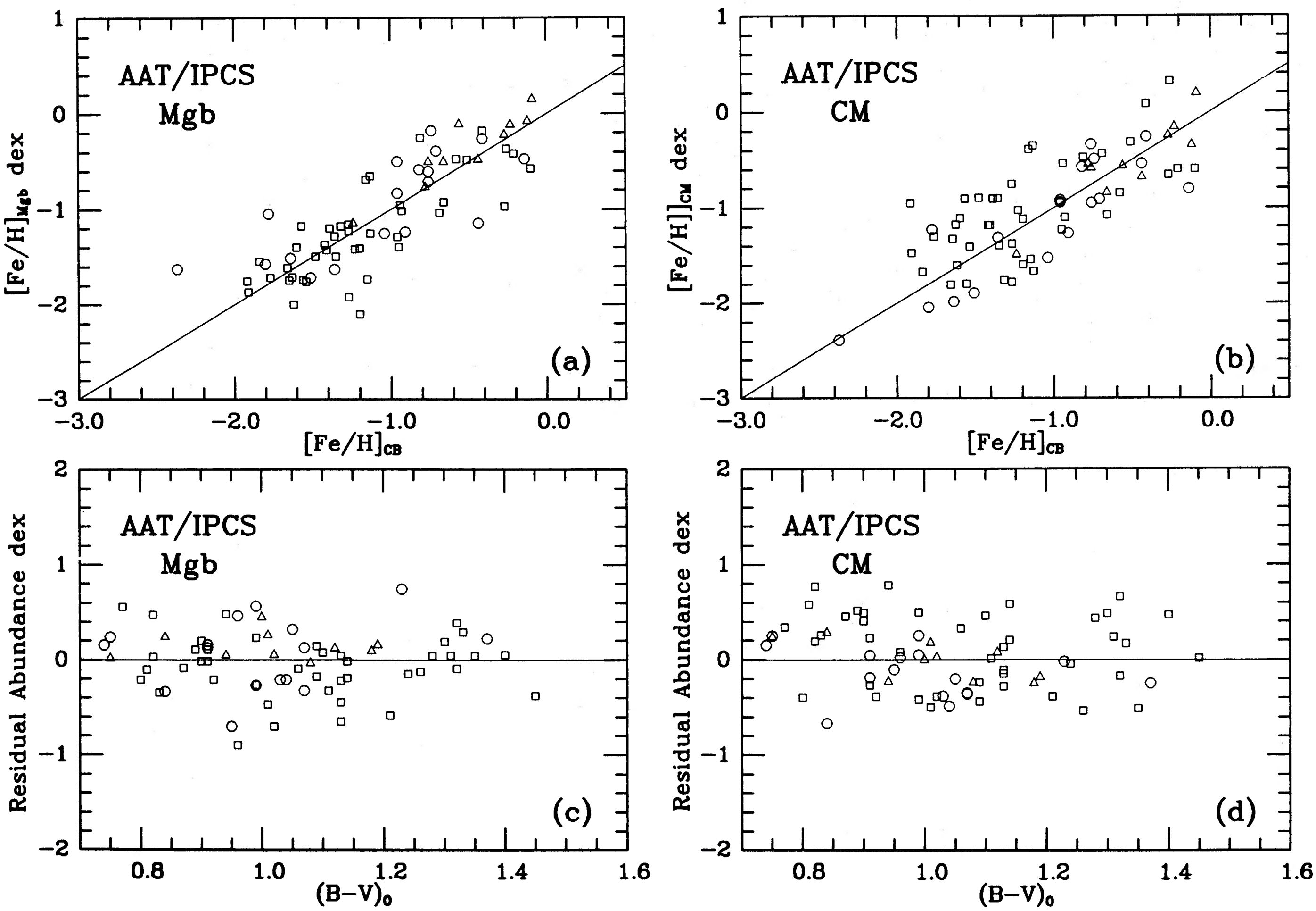

FIG. 6.—Figs. 6a and 6b show the dependence of the Mg*b* index and the CM index on $[Fe/H]_{CB}$. Figs. 6c and 6d show the residuals in the sense $[Fe/H]_{Mgb} - [Fe/H]_{CB}$ etc. against $(B-V)_0$. The circles, triangles, and squares represent observations in the three fields SA 141, SA 189, and SA 127, respectively.

for a giant and dwarf respectively. As usual, three categories are needed: Sr II stronger or equal strength (indicating a giant), Fe I much stronger (indicating a dwarf), and stars difficult to classify clearly into either of these two categories. Other criteria are needed to classify these ambiguous stars. Corresponding spectra in the green region from the same observations are shown in Figures 9*b* and 9*d*. We reject any star showing even a weak MgH band in its spectrum.

For the MSO/B2PCA spectra, this Sr II/Fe I classification is not possible. In the blue spectra, the Canberra night sky Hg line at 4077 Å makes the Sr II/Fe I criterion difficult to apply with any confidence. In order to make use of the MSO spectra for the analysis, we examine the CB and CM + Mg*b* abundance estimates for the contaminating dwarfs identified in our sample from the IPCS spectra and the Sr II/Fe I classification. These abundance estimates are shown in Figure 10*a*. We see that all of these dwarfs (*filled symbols*) have formal values of $[Fe/H]_{CB} > 0$ and $[Fe/H]_{CM+Mgb} > -0.1$. To err on the conservative side and ensure that our sample is not contaminated (at the expense of losing some metal strong giants), we reject from our current sample all stars observed only at MSO which show $[Fe/H]_{CB} > -0.3$ or $[Fe/H]_{CM+Mgb} > -0.3$. The stars which show $+0.2 > [Fe/H] > -0.3$ will be reobserved later to recover any rejected giants. We have also decided to reject the few stars with $[Fe/H] > 0$ for which the Sr II classification from the IPCS spectra is not clear (*star symbols*), because they are probably contaminating dwarfs. A similar plot, in which stars classified as dwarfs from the MgH band criterion are shown as filled symbols, is given in Figure 10*b*.

At this stage, we summarize the criteria which we have used to produce a sample of giants uncontaminated by foreground dwarfs. From the photographic photometry and objective prism spectra, we select for improved photometry and slit spectroscopy those stars with $(B-V)_{pg} > 0.9$ and no visible MgH features. We then exclude from the sample, on any one of the following, any star which (1) is rejected by the Sr II/Fe I criterion; (2) shows any MgH irrespective of color [we recognize that some relatively metal strong giants $[Fe/H] > -0.7$ and $(B-V)_0 > 1.2$ will be rejected by this criterion]; (3) was observed only at MSO and shows $[Fe/H]_{CB} > -0.3$ or $[Fe/H]_{CM+Mgb} > -0.3$; (4) has $(B-V)_0 < 0.8$ and is in group *a*; (5) has $(B-V)_0 < 0.9$ and is in group *b*; (6) has an absolute magnitude $M_V > +3$ (derived from its abundance and color). [In the above, $(B-V)_0$ denotes dereddened photoelectric or spectrophotometric color.] The adopted reddening for each field is given in Table 1: see RF1.

As a further check on the validity of our selection procedure, we examine the kinematics of the sample. Figure 11*a* shows that the stars (*filled symbols*) rejected as disk dwarfs, with formal values of $[Fe/H] > 0$, have a small line-of-sight velocity

TABLE 1

OBSERVATIONS OF FIELD HALO K GIANTS

Identity	l	b	V	$(B-V)_0$	M_V	[Fe/H]	D (kpc)	V_{los} (km s^{-1})	Observation
SA 141: $E(B-V) = 0.00$									
−290105E	244.2	−85.0	13.58	0.91	1.3	−0.9	2.9	−27	AAT/IPCS
−300100A	256.5	−85.9	14.40	1.37	−2.2	−1.8	20.6	−24	AAT/IPCS
−290100C	252.5	−86.7	15.27	0.94	0.3	−1.3	10.0	−67	AAT/IPCS
−300100B	251.8	−85.7	15.59	1.04	−0.3	−1.2	15.1	−18	AAT/IPCS
−300055A	265.5	−86.5	14.57	1.71	−2.1	−1.5	21.7	8	AAT/IPCS
−310115A	248.8	−82.2	15.96	0.99	−0.3	−1.4	18.3	−40	AAT/IPCS
−320100A	275.4	−84.7	15.71	1.03	−1.0	−1.7	21.7	−63	AAT/IPCS
−300100F	262.7	−85.9	15.08	1.18	−0.8	−1.1	14.6	1	AAT/IPCS
−290105B	236.0	−85.7	13.48	0.96	0.9	−0.8	3.2	63	AAT/IPCS
−290105G	241.7	−85.6	13.92	0.91	1.6	−0.8	2.9	81	AAT/IPCS
−290105H	243.8	−85.6	13.71	1.05	0.6	−0.7	4.3	0	AAT/IPCS
−300105A	250.4	−85.6	13.64	0.99	1.3	−0.5	3.0	−31	AAT/IPCS
−310100A	262.8	−85.2	13.22	1.07	−1.2	−1.7	7.7	35	AAT/IPCS
−300115B	245.2	−83.3	13.24	1.23	−2.4	−2.2	13.3	91	AAT/IPCS
−280100A	231.4	−87.2	14.38	1.07	−0.2	−1.1	8.4	116	AAT/IPCS
−310110A	250.4	−83.4	14.19	0.95	1.5	−0.6	3.5	60	AAT/IPCS
−270115A	220.2	−84.1	15.72	1.03	−0.4	−1.3	16.9	−19	AAT/IPCS
−310100C	270.5	−85.4	15.22	0.87	0.9	−1.3	7.4	18	AAT/IPCS
−290110D	235.9	−84.0	15.52	1.04	0.0	−1.0	12.8	169	AAT/IPCS
−300110C	245.6	−84.1	15.70	1.04	−0.1	−1.1	14.7	−20	AAT/IPCS
−300115A	240.0	−82.6	15.69	1.07	−0.2	−1.1	15.1	1	AAT/IPCS
−290110C	241.6	−84.2	13.32	1.27	−1.7	−1.6	10.1	−147	MSO/B2PCA
−290110A	237.7	−84.9	14.05	0.94	0.4	−1.2	5.2	10	MSO/B2PCA
−290100E	247.5	−85.9	13.40	0.86	2.4	−0.7	1.6	−65	MSO/B2PCA
−290105N	238.5	−84.9	14.49	1.05	0.4	−0.8	6.5	−6	MSO/B2PCA
−290055C	257.4	−86.8	14.38	1.05	−0.9	−1.6	11.5	18	MSO/B2PCA
−290055D	262.6	−86.8	13.98	1.05	−0.8	−1.5	9.2	0	MSO/B2PCA
−290055E	259.2	−86.8	14.04	0.94	1.1	−0.8	3.8	27	MSO/B2PCA
−310110B	255.1	−83.0	13.38	0.90	1.9	−0.7	2.0	−7	MSO/RSPCA
−310110C	253.0	−83.6	13.34	1.04	0.6	−0.7	3.5	89	MSO/R2PCA
−290115A	232.3	−83.0	13.93	1.27	−1.6	−1.5	12.6	−205	MSO/R2PCA
−300115C	239.0	−83.6	13.64	0.93	1.3	−0.8	3.0	37	MSO/RSPCA
SA 189: $E(B-V) = 0.00$									
−590310B	275.5	−49.9	13.66	1.02	1.6	−0.3	2.6	32	AAT/IPCS
−610320C	276.7	−47.8	13.42	1.18	−1.0	−1.3	7.6	114	AAT/IPCS
−590300B	277.4	−50.5	13.56	1.01	1.8	−0.2	2.3	−17	AAT/IPCS
−580310B	273.2	−49.7	13.41	1.12	1.0	−0.2	3.1	44	AAT/IPCS
−580310A	274.0	−49.3	15.03	1.01	0.9	−0.6	6.7	99	AAT/IPCS
−580250G	276.1	−52.1	15.74	0.93	−0.3	−1.6	16.3	46	AAT/IPCS
−600250M	278.6	−51.0	15.56	1.29	−1.1	−1.1	21.1	73	AAT/IPCS
−600320L	274.8	−47.7	15.30	1.01	−0.7	−1.5	15.6	328	AAT/IPCS
−580300D	274.7	−50.9	15.16	0.99	−1.1	−1.9	18.2	36	AAT/IPCS
−610250G	281.3	−50.1	15.97	1.06	−0.5	−1.3	20.0	156	AAT/IPCS
−600320G	275.4	−48.0	15.15	1.08	0.7	−0.5	7.9	102	AAT/IPCS
−580320B	273.3	−49.3	14.78	1.00	1.4	−0.4	4.8	55	AAT/IPCS
−600320J	276.3	−47.7	14.89	0.94	2.6	−0.2	2.8	−21	AAT/IPCS
−610300C	279.4	−49.3	15.06	1.19	−0.1	−0.7	10.9	107	AAT/IPCS
−600250A	278.3	−50.2	13.73	1.17	−1.0	−1.3	8.9	64	MSO/R2PCA
−600250C	279.1	−50.2	13.94	0.98	1.6	−0.4	3.0	95	MSO/R2PCA
SA 127: $E(B-V) = 0.03$									
−161110B	272.6	40.2	13.96	1.31	−1.4	−1.4	11.5	233	AAT/IPCS
−191110D	273.5	37.9	13.85	0.89	1.1	−1.1	3.5	294	AAT/IPCS
−171105A	271.6	39.1	14.82	1.45	−2.2	−1.7	24.3	214	AAT/IPCS
−181055A	270.1	36.9	15.04	1.24	−1.3	−1.4	18.0	259	AAT/IPCS
−171115A	274.8	40.1	14.78	1.28	−2.0	−1.8	21.4	212	AAT/IPCS
−181115A	275.0	39.7	14.36	1.63	−2.3	−1.6	20.7	84	AAT/IPCS
−191110E	273.5	37.7	14.52	1.09	−1.2	−1.7	13.6	295	AAT/IPCS
−171100C	270.1	38.5	14.24	1.13	−1.2	−1.6	11.9	−100	AAT/IPCS
−171100D	270.2	38.2	15.11	1.21	−1.2	−1.4	17.9	72	AAT/IPCS
−191105B	272.5	36.7	14.92	1.11	−0.4	−1.0	11.0	−46	AAT/IPCS
−191105C	272.2	36.8	14.30	1.33	−2.0	−1.7	17.3	237	AAT/IPCS
−171100E	270.0	38.1	14.83	1.40	−2.0	−1.6	22.5	267	AAT/IPCS
−171100A	270.9	38.3	15.15	1.06	−1.0	−1.6	16.3	286	AAT/IPCS
−191115D	274.8	38.3	14.81	1.30	−1.2	−1.2	15.6	147	AAT/IPCS
−191110A	274.3	38.0	15.55	1.13	−1.1	−1.5	20.3	65	AAT/IPCS

TABLE 1—*Continued*

Identity	l	b	V	$(B-V)_0$	M_V	[Fe/H]	D (kpc)	V_{los} (km s^{-1})	Observation
			SA 127: $E(B-V) = 0.03$—*Cont.*						
−171100I	270.8	38.0	15.65	1.32	−1.4	−1.3	24.7	94	AAT/IPCS
−161115C	273.6	40.5	15.79	1.13	−0.6	−1.1	18.1	257	AAT/IPCS
−161110D	271.8	40.5	15.45	0.99	1.9	−0.2	4.9	−49	AAT/IPCS
−161110A	272.7	40.3	15.17	1.10	−0.6	−1.2	13.8	12	AAT/IPCS
−171100H	269.7	37.6	15.06	0.91	0.4	−1.4	8.4	105	AAT/IPCS
−191110C	273.7	37.7	14.92	1.14	−0.8	−1.2	13.2	251	AAT/IPCS
−171115E	274.0	39.5	15.51	0.90	0.3	−1.4	10.6	187	AAT/IPCS
−161100C	269.7	38.7	15.35	0.87	0.4	−1.5	9.5	−11	AAT/IPCS
−161100A	269.2	38.6	15.11	1.32	−1.0	−1.0	15.9	−4	AAT/IPCS
−181100A	271.1	38.0	14.96	1.14	−0.9	−1.3	14.5	295	AAT/IPCS
−181100B	271.3	37.7	15.02	0.94	1.2	−0.8	5.6	83	AAT/IPCS
−191055A	270.9	35.8	14.73	0.90	1.5	−0.8	4.2	124	AAT/IPCS
−161105E	270.5	39.1	15.46	0.80	1.6	−1.4	5.7	277	AAT/IPCS
−171105H	271.8	38.6	15.22	0.82	2.6	−0.9	3.2	−38	AAT/IPCS
−171110F	272.1	39.6	15.40	0.83	2.8	−0.7	3.2	12	AAT/IPCS
−181105K	272.7	38.1	15.35	0.96	−0.1	−1.4	11.9	374	AAT/IPCS
−171115B	273.6	39.8	15.33	1.01	1.5	−0.3	5.6	76	AAT/IPCS
−171110B	273.0	39.3	15.67	1.09	−0.8	−1.4	19.1	233	AAT/IPCS
−181110B	273.4	38.1	15.27	1.02	1.0	−0.5	6.8	40	AAT/IPCS
−191120A	275.9	38.5	15.64	0.99	0.7	−0.8	9.3	28	AAT/IPCS
−191115E	275.5	37.1	15.60	1.26	−1.2	−1.3	22.4	287	AAT/IPCS
−181105E	271.6	38.2	15.56	0.92	2.4	−0.4	4.1	115	AAT/IPCS
−191105D	273.1	37.3	15.06	1.35	−1.6	−1.4	20.4	129	AAT/IPCS
−191105F	272.6	37.1	15.39	1.13	−1.4	−1.7	22.0	3	AAT/IPCS
−171115F	273.8	40.0	15.30	0.91	1.9	−0.6	4.5	56	AAT/IPCS
−161110F	272.6	40.4	13.69	1.12	0.6	−0.4	4.1	101	MSO/B2PCA
−161115A	274.2	40.8	14.55	1.18	−0.1	−0.6	8.0	6	MSO/B2PCA
−161115B	273.9	40.8	14.19	1.11	−0.8	−1.3	9.7	316	MSO/B2PCA
−161110C	271.8	40.5	13.56	1.05	0.0	−1.0	5.0	−1	MSO/B2PCA
−191115B	275.2	38.5	14.52	1.00	1.5	−0.4	3.8	51	MSO/B2PCA
−161105A	271.0	39.7	14.47	1.05	0.0	−1.0	7.4	150	MSO/B2PCA
−161110E	271.7	40.4	13.77	1.14	−0.5	−1.0	6.8	231	MSO/B2PCA
−191115A	275.6	38.8	14.03	1.15	0.1	−0.6	5.9	44	MSO/B2PCA
−181110D	273.0	38.0	14.68	1.02	0.6	−0.8	6.3	219	MSO/R2PCA
−171100L	270.0	37.8	14.46	0.93	2.3	−0.3	2.6	75	MSO/R2PCA
−181105H	271.7	37.3	14.14	1.05	0.5	−0.7	5.2	155	MSO/R2PCA
−181100E	270.3	37.7	14.23	1.07	1.0	−0.3	4.2	−74	MSO/R2PCA
−191105E	273.1	36.8	14.33	1.23	−0.7	−0.9	9.6	99	MSO/R2PCA
−171100B	270.5	38.2	13.81	1.07	−0.2	−1.1	6.1	149	MSO/R2PCA
−191105A	273.1	37.2	13.77	1.02	1.0	−0.5	3.4	22	MSO/R2PCA
−181100K	269.9	37.4	14.90	1.22	−0.8	−1.0	13.0	389	MSO/R2PCA
−161100D	269.2	39.4	14.81	1.20	0.8	0.0	6.1	73	MSO/R2PCA
−171100J	270.8	38.2	14.01	1.15	0.9	−0.1	4.0	34	MSO/R2PCA

dispersion (about 30 km s^{-1}); this is consistent with membership of the disk population and is clearly different from the velocity dispersion of the stars accepted as giant stars of the spheroidal population.

Figures 12*a* and 12*b* show the metal abundance of our giants against their magnitude V and color $(B-V)_0$. The filled symbols represent stars classified on the objective prism spectra as having strong Mg*b* (but no MgH). Most of these stars are relatively metal strong, with [Fe/H] > -1. The few with [Fe/H] < -1 are red and faint. This is not surprising, because the cooler stars have stronger lines. Also, for the faintest stars, spurious features near Mg*b* in the noisier objective prism images could be mistaken for the Mg*b* lines. We also note that none of the bluer, metal weaker giants, with $(B-V) < 1.0$ and [Fe/H] < -1, have been classified as Mg*b*-strong. This fact will be useful in the future when we extend our survey to the bluer color range $0.7 < (B-V) < 0.9$, in order to identify the intrinsically fainter metal weak giants with [Fe/H] < -1; most of these are now excluded by the $(B-V) = 0.9$ color limit of this first survey.

Figure 13*a* shows the color–apparent magnitude distribution of our giants; its only feature is the absence of bluer stars around $V \approx 14.5$, which comes from the way in which we have chosen stars for slit spectroscopy at the two telescopes. Figure 13*b* shows the color–absolute magnitude distribution of our giants. The broken lines denote empirical giants branches for [Fe/H] = 0.0 and −2.0, interpolated from the grid of observed cluster giant branches used to estimate the photometric parallaxes of our stars (see RF1). We see that the stars classified as strong Mg*b* occupy the metal-strong lower edge of the red giant branch. Again, none of the giants with $(B-V) < 1$ and $M_V < +1$ show strong Mg*b*.

How does this new analysis change the catalog of RF1 (their Table 1)? Of the 33 stars in SA 141 (−300105F was duplicated in the list by error), 24 of them remain. Of the nine rejected stars, (1) two are rejected because our observations of stars with $V > 15$ at MSO are unsuitable (due to sky noise) for our new abundance estimates; (2) three have $M_V > +3$; (3) four are rejected on our other revised selection criteria. Six stars which were excluded from RF1 are now included; with four

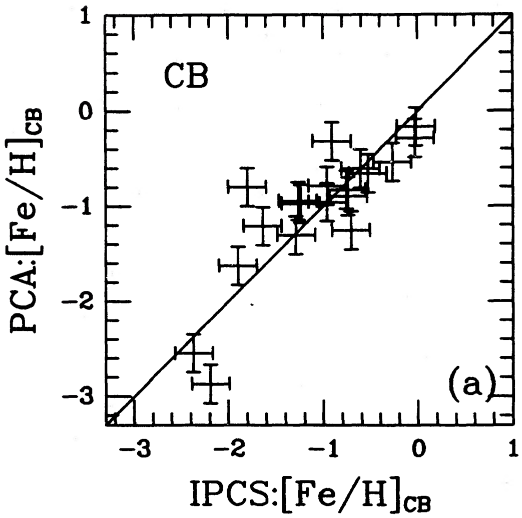

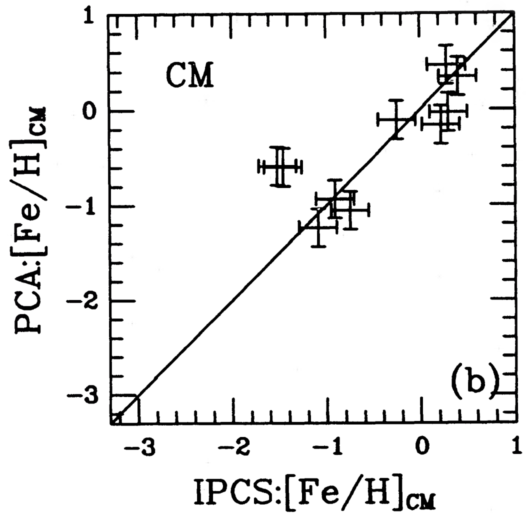

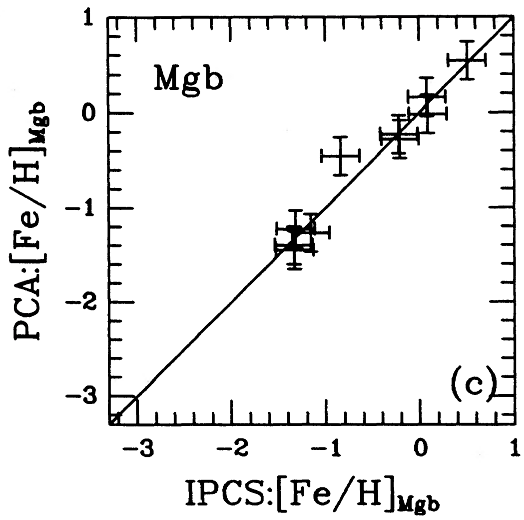

FIG. 7.—Figs. 7*a*, 7*b*, and 7*c* compare the abundances of stars measured at MSO using CB, CM, and Mg*b* indices, respectively, against the corresponding AAT/IPCS abundances for stars measured at both the AAT and MSO. The diagonal line in each panel is the one-to-one relation.

giants from new spectroscopic observations, we now have 34 giants in the SA 141 field.

Of the 19 stars in SA 189, 10 of them remain. Of the nine rejected stars, (1) three are rejected because reanalysis shows that the radial velocities from the MSO observations on 1982 September 9 are not reliable, due to technical problems; (2) one has $(B-V) < 0.8$; (3) five get rejected on our other revised selection criteria. With six giants from new observations, we now have 16 giants in the SA 189 field.

Of the 39 stars in SA 127, only one was rejected; two were accepted back on our revised selection criterion. With 18 giants from new observations, we now have 58 giants in the SA 127 field.

As a result of this fairly rigorous procedure for excluding dwarfs from our sample, we believe that all of the stars in Table 1 of this paper are giants. As a final check, Chris Flynn and Heather Morrison kindly obtained DDO photometry with the 2.3 m telescope at Siding Spring Observatory for several of our stars with the least certain classifications. All of these stars were confirmed to be giants.

IV. KINEMATICS AND ABUNDANCES

Our new estimates of absolute magnitude, abundance and distance are given in Table 1 for all the halo giants measured by us so far, and supersedes Table 1 of RF1 (and therefore also the values tabulated for our stars by Norris 1986). The samples here are not complete, as many halo giant candidates identified in the survey have not yet been observed spectroscopically. Photoelectric or spectrophotometric $(B-V)$ colors are now available for all the stars in the catalog. Our data was entirely reanalyzed, using the procedures described above, and small adjustments were made to the velocity zero-points. Because we have now observed more stars, the reanalysis was justified to ensure that all our data are on the same system.

Our procedure for estimating absolute magnitude and thus distance to our giants is described in the appendix. Distance

1989ApJ...339..126R

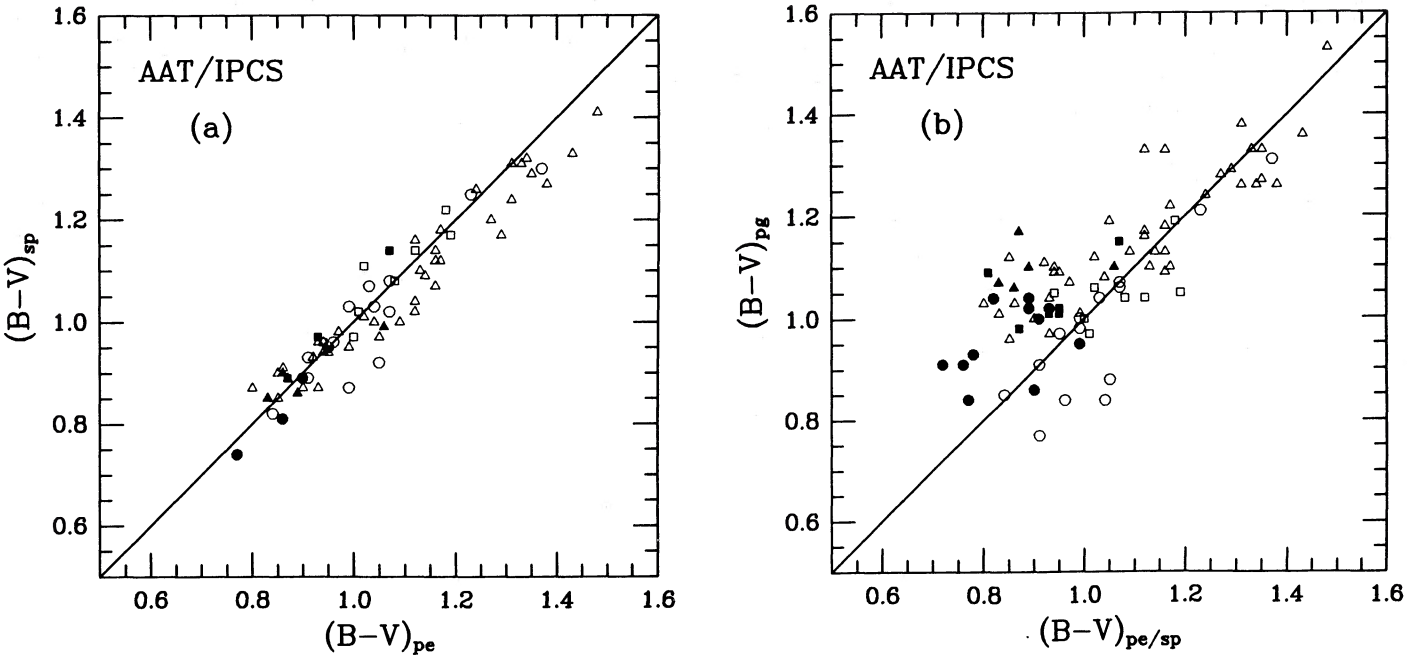

FIG. 8.—(*a*) Comparison of the spectrophotometric $(B-V)$ with photoelectric $(B-V)$. The rms scatter is 0.05 mag. The symbols identify the accepted giants (*open*) and rejected dwarfs (*filled*) in SA 141, SA 189, and SA 127. Other coding as in Fig. 6. (*b*) Comparison of the photoelectric or spectrophotometric $(B-V)$ values with the original photographic colors. This shows the bias introduced by the objective prism selection procedure in favor of dwarfs which are bluer than their estimated $(B-V)_{pg}$.

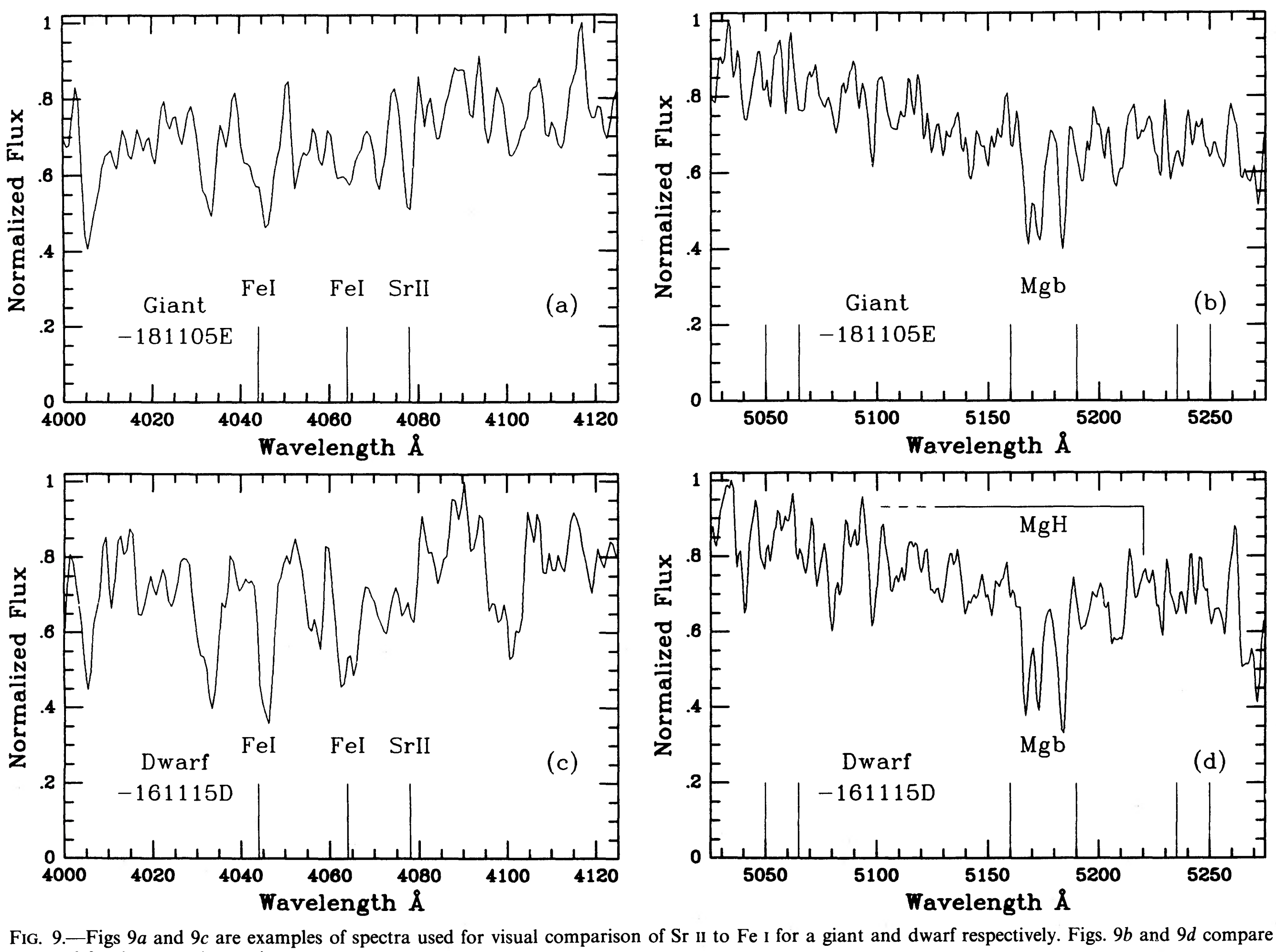

FIG. 9.—Figs 9*a* and 9*c* are examples of spectra used for visual comparison of Sr II to Fe I for a giant and dwarf respectively. Figs. 9*b* and 9*d* compare the MgH + Mg*b* for the same observations.

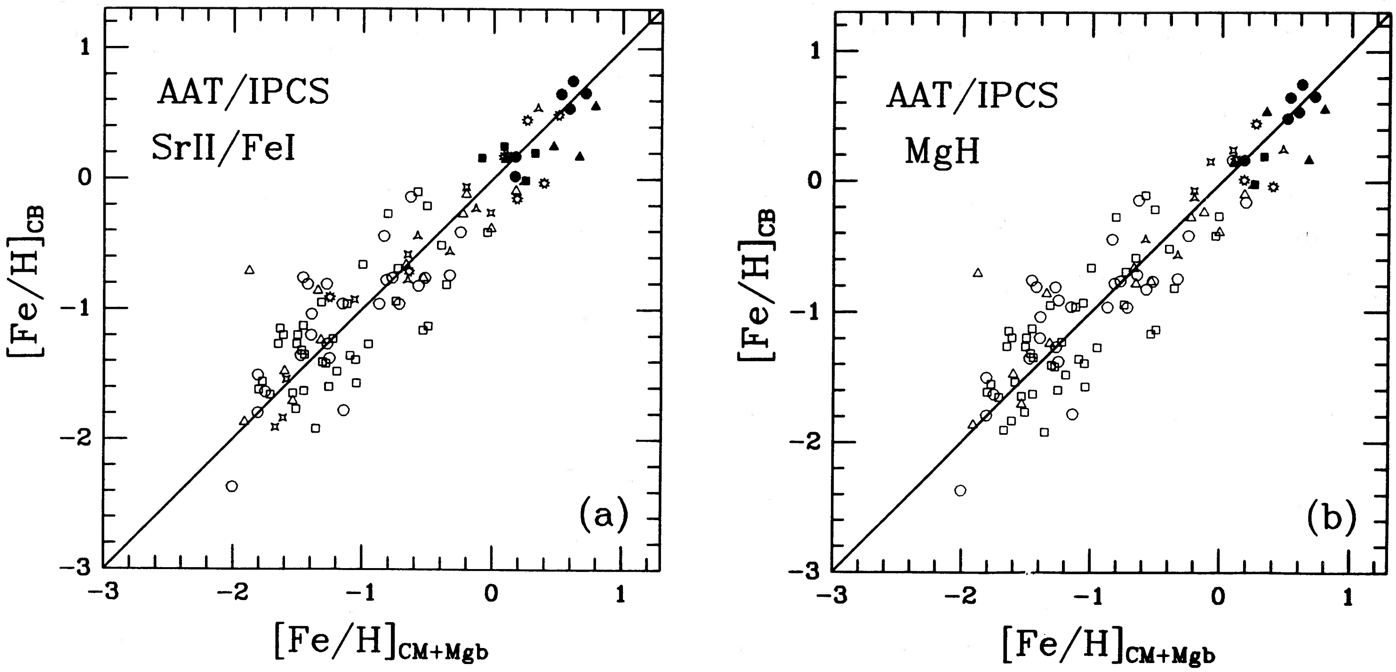

FIG. 10.—(*a*) $[Fe/H]_{CB}$ against $[Fe/H]_{CM+Mgb}$ from IPCS spectra. Stars identified as dwarfs from the Sr II/Fe I criterion are shown as filled symbols: uncertain classifications are shown as starred symols. Other coding as in Fig. 6. (*b*) As in Fig. 10*a* but with stars identified as dwarfs from the MgH criterion shown as filled symbols.

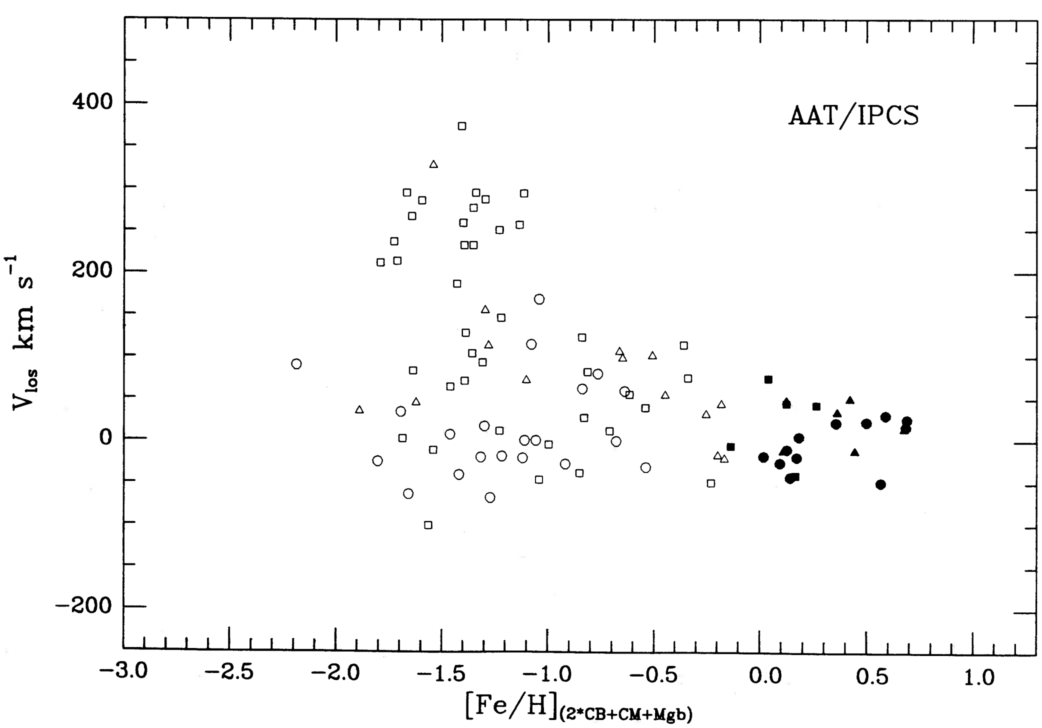

FIG. 11.—Line-of-sight velocities for the sample show that the rejected dwarfs (*filled symbols*) have a velocity dispersion of about 30 km s^{-1}, consistent with that of the old disk population and different from the sample accepted as belonging to the spheroidal population. Other coding as in Fig. 6.

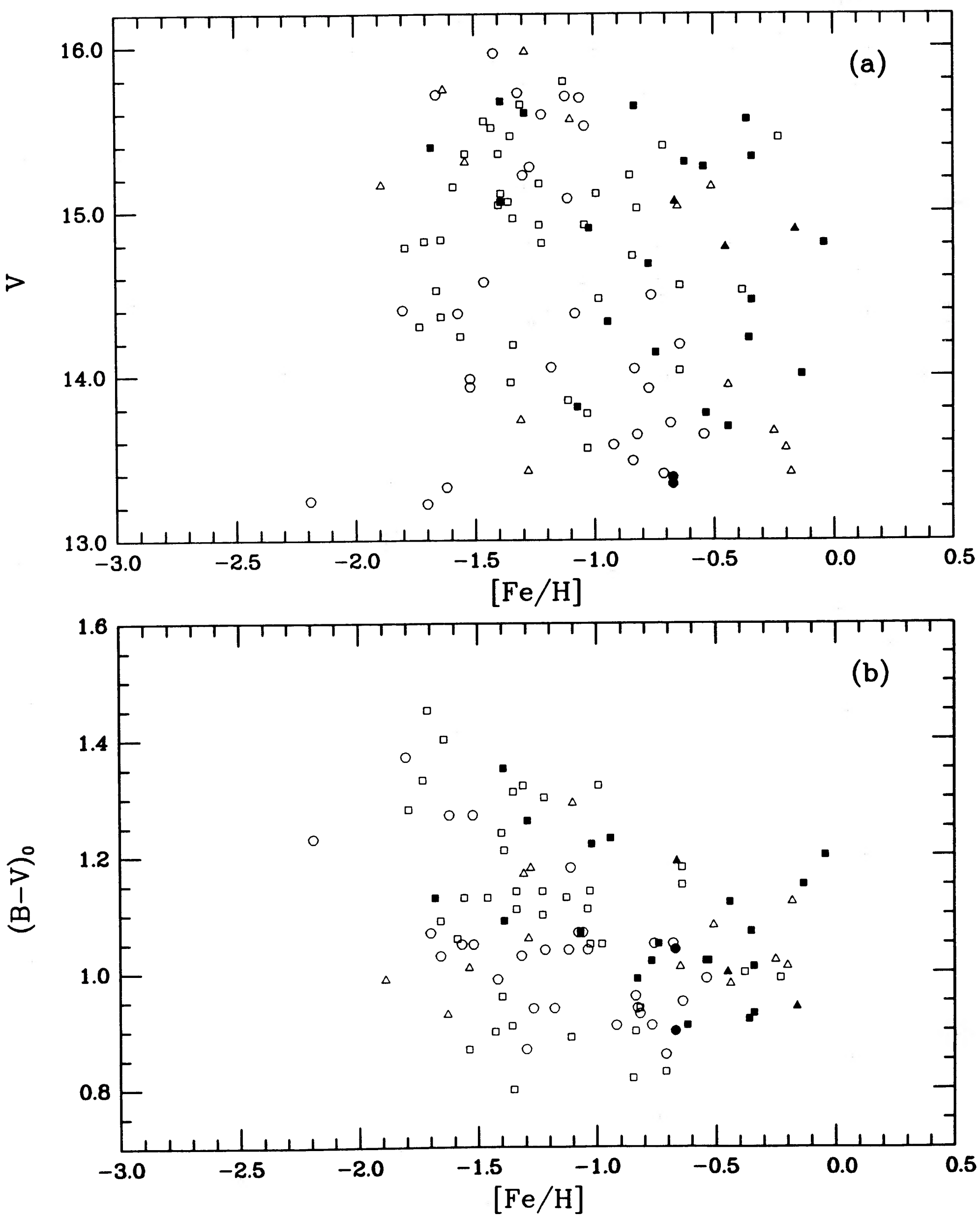

FIG. 12.—Metal abundance distribution of our giants against (*a*) *V* magnitude and (*b*) $(B-V)_0$. Open symbols are stars with no visible Mg*b* (group *a*). Filled symbols are stars with clearly visible Mg*b* in their objective prism spectra (group *b*). Other coding as in Fig. 6. None of the giants with $(B-V)_0 < 1.0$ and [Fe/H] < -1 are in group *b*.

errors were estimated using a Monte Carlo procedure and are shown in Figures 20*a* and 20*b* as a function of distance and $(B-V)_0$. Typical fractional distance errors are 0.12 for the AAT data ([Fe/H] $\pm$ 0.15 dex) and 0.25 for the PCA data ([Fe/H] $\pm$ 0.3 dex).

Figures 14–16 show the main results for our SA 141 and SA 127 fields. Because there are so few stars from the SA 189 field in our catalog, we will not discuss this field any further, except to summarize its properties in Table 2. Further spectroscopic and photometric work is in progress on the SA 189 field and will be published later. Circles, triangles, and squares identify observations with the AAT/IPCS, MSO/B2PCA, and MSO/R2PCA, respectively. (Over 70% of the observations were made with the AAT/IPCS system.) Filled symbols represent stars with [Fe/H] ≥ -0.7, as explained below.

Figure 14 shows the kinematics of the giants as a function of metal abundance in the two fields. In the SA 127 field we now see that the more metal strong giants, with [Fe/H] ≥ -0.7, have a much smaller velocity dispersion and a smaller mean velocity than the more metal weak giants. This difference was not apparent in RF1, because it was masked by errors in our Ca II abundances and also because data for many of the metal stronger giants were not available at that time. The kinematical difference between these relatively distant metal weak and metal strong giants is particulary interesting: it is similar to the differences found by Zinn (1985) in the kinematics of the

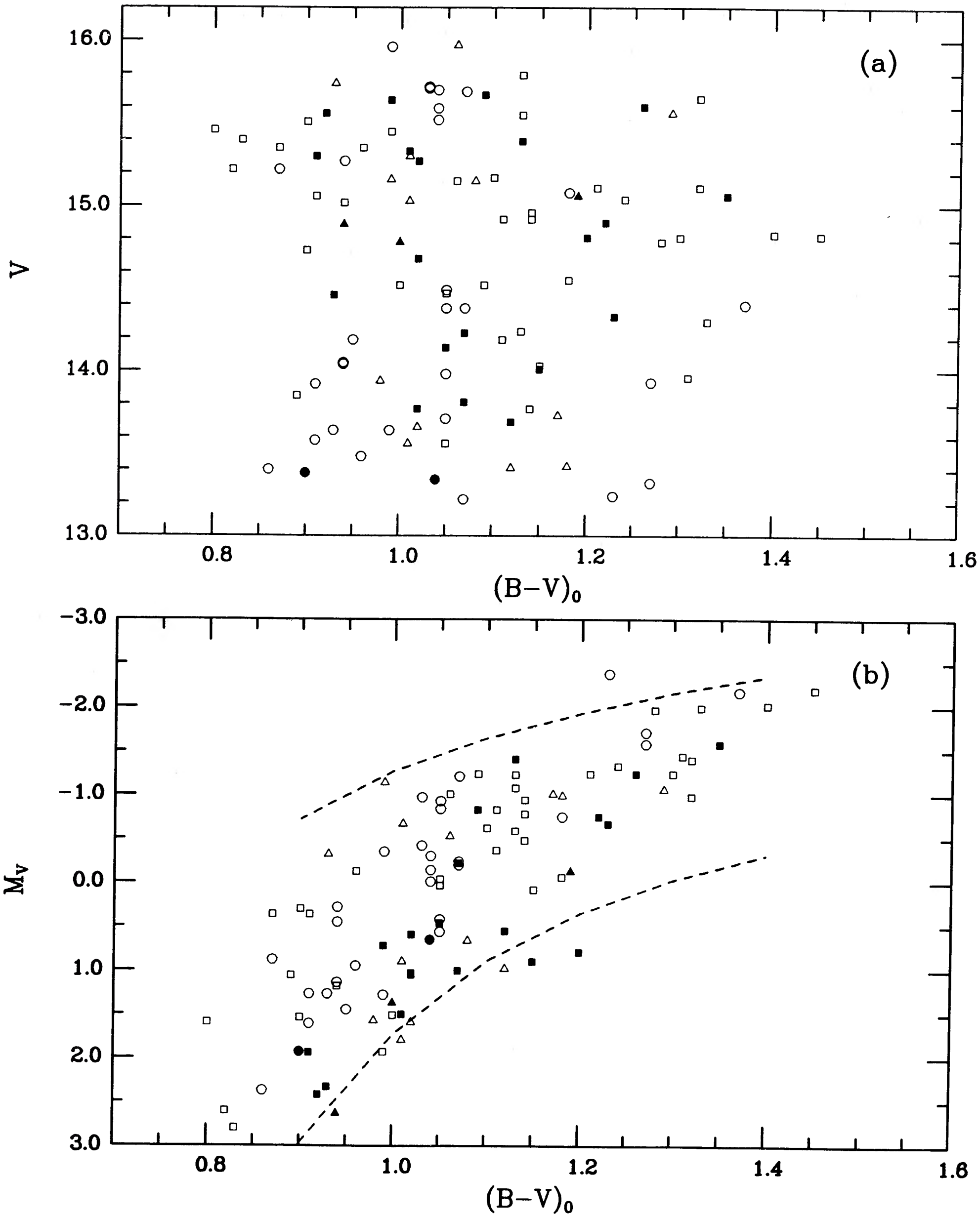

FIG. 13.—(*a*) Color–apparent magnitude and (*b*) color–absolute magnitude distribution of the giants. The stars with clearly visible Mg*b* in their objective prism spectra (group *b*) occupy the metal-strong lower edge of the red giant branch. We again see that none of the giants with $(B-V) < 1.0$ and $M_V < +1$ are in group *b*. Coding as in Fig. 12.

metal-weak and metal-strong globular clusters. The division between the two populations is found at about the same abundance, [Fe/H] ≈ -0.7, for the globular clusters and for our field giants.

Figure 15 shows the kinematics of these giants against distance D from the Sun. The distance interval is limited by both the apparent magnitude and the color limits of the survey: $13 < V < 16$ and $(B-V) > 0.9$. The main feature of this figure is the marked difference in the line of sight velocity dispersion observed for the metal weak giants toward the SGP (SA 141) and towards SA 127; this difference was already noted by RF1. However, because of the revised distance estimates associated with the improved abundances, the run of velocity dispersion with distance towards the SGP is slightly different here from that given by RF1. Some of the lower velocity stars with estimated distances around 10 kpc turn out now to be closer to the Sun, resulting in a larger estimate for the velocity dispersion at that height. The numbers of halo giants in this SGP field is still small, and the run of velocity dispersion with distance is not yet well determined (see below). We note without further comment the similar velocity and abundance for the four giants at a distance of about 15 kpc in the SA 141 field.

Figure 16 illustrates the distribution of abundance with distance from the Sun for the giants in the two fields. Because of the survey limits in color and apparent magnitude, our stars are confined to the region between the two dashed curves. The metal stronger giants are found only between about 2 and 5 kpc above the Galactic plane, in both fields, although we would discover them to much greater heights if they were there. The sample of metal-weak spheroid giants shows no

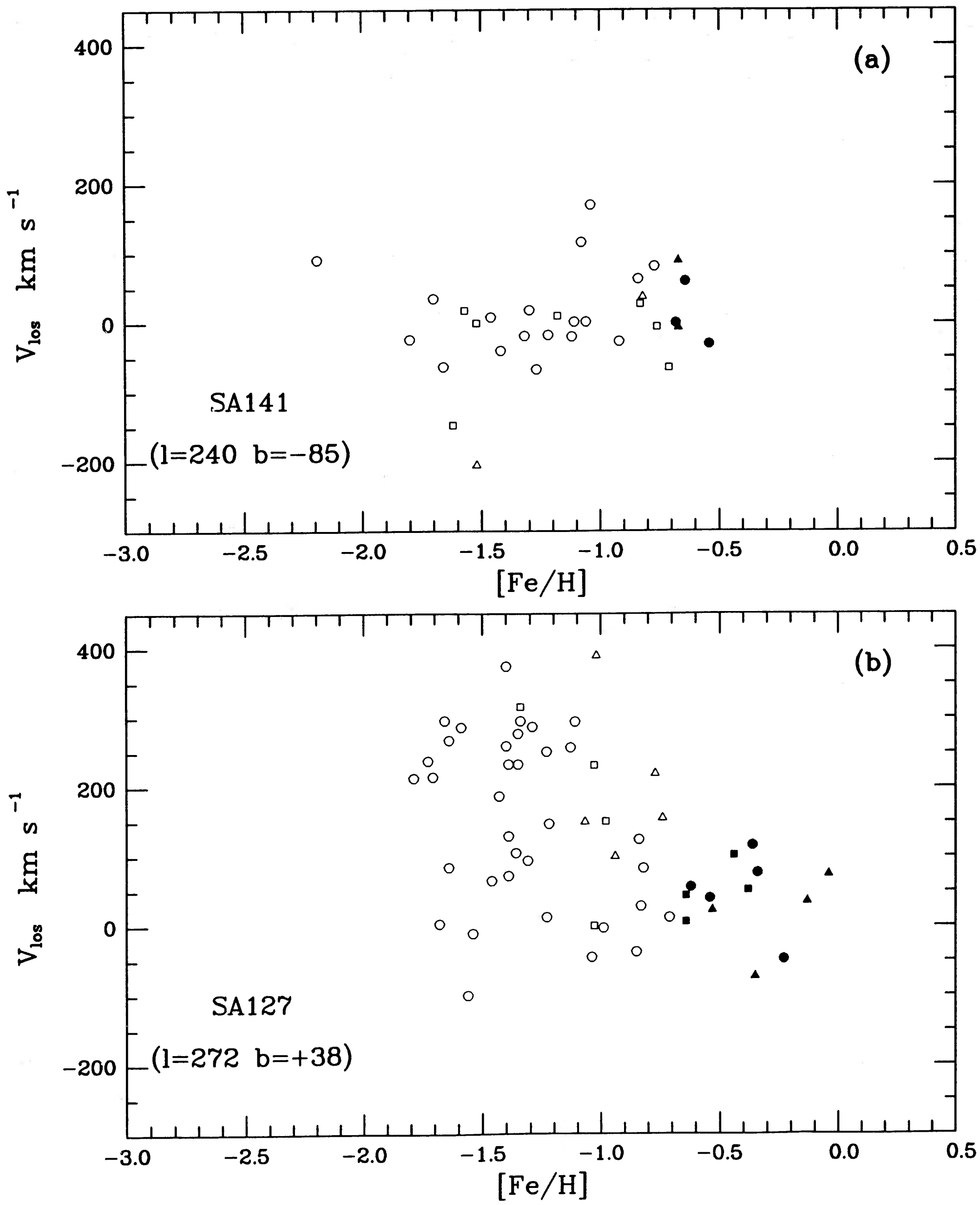

FIG. 14.—Kinematics of the giants as a function of metal abundance for our two best observed fields, SA 141 and SA 127. Note the much smaller velocity dispersion and mean velocity of the metal stronger giants (*filled symbols*) in SA 127. We use a separating abundance of [Fe/H] = −0.7. Circles, triangles, and squares identify observations, with the AAT/IPCS, MSO/B2PCA, and MSO/R2PCA, respectively.

clear abundance gradient beyond a distance of about 10 kpc from the Sun (11 kpc cylindrical radius from the Galactic center in the SA 127 direction).

Table 2 gives the mean properties of some subsamples of giants in the three fields. We partition the sample first into the two abundance bins [Fe/H] > -0.7 and [Fe/H] ≤ -0.7, as suggested by Figure 14*b*. The metal strong giants (denoted TD in Table 2) are all within 8 kpc of the Sun, and we consider them as a single sample. The more metal weak giants (SA) are further partitioned into three subsamples at near (SN), intermediate (SI), and far (SF) distances, to examine the variation of the line-of-sight velocity dispersion with distance. The columns in Table 2 are, respectively, the subsample identification, the number of giants, the mean distance $\langle D \rangle$, mean height $\langle z \rangle$ above the Galactic plane, mean distance $\langle R \rangle$ from the Galactic center, mean absolute magnitude $\langle M_V \rangle$, mean abundance $\langle$[Fe/H]$\rangle$, mean line-of-sight velocity $\langle V_{los} \rangle$ [corrected for the Sun's peculiar motion (9, 12, 7) km s^{-1}], and the line-of-sight velocity dispersion σ_{los}.

From Table 2, the mean velocity for stars at the SGP (SA 141) is near zero, as expected, and we evaluate the dispersions assuming a zero mean. We consider first the kinematics of the metal-weak giants. The velocity dispersion of the nearer metal-weak K giants (up to 6 kpc) is 48 ± 13 km s^{-1}, consistent within the errors with the value from Beers, Preston, and Shectman (1985) of 60 km s^{-1} for metal-weak giants at a mean distance of 2 kpc, and with Pier's (1983) value of 61 km s^{-1} for BHB stars at a mean distance of 6 kpc. For comparison with

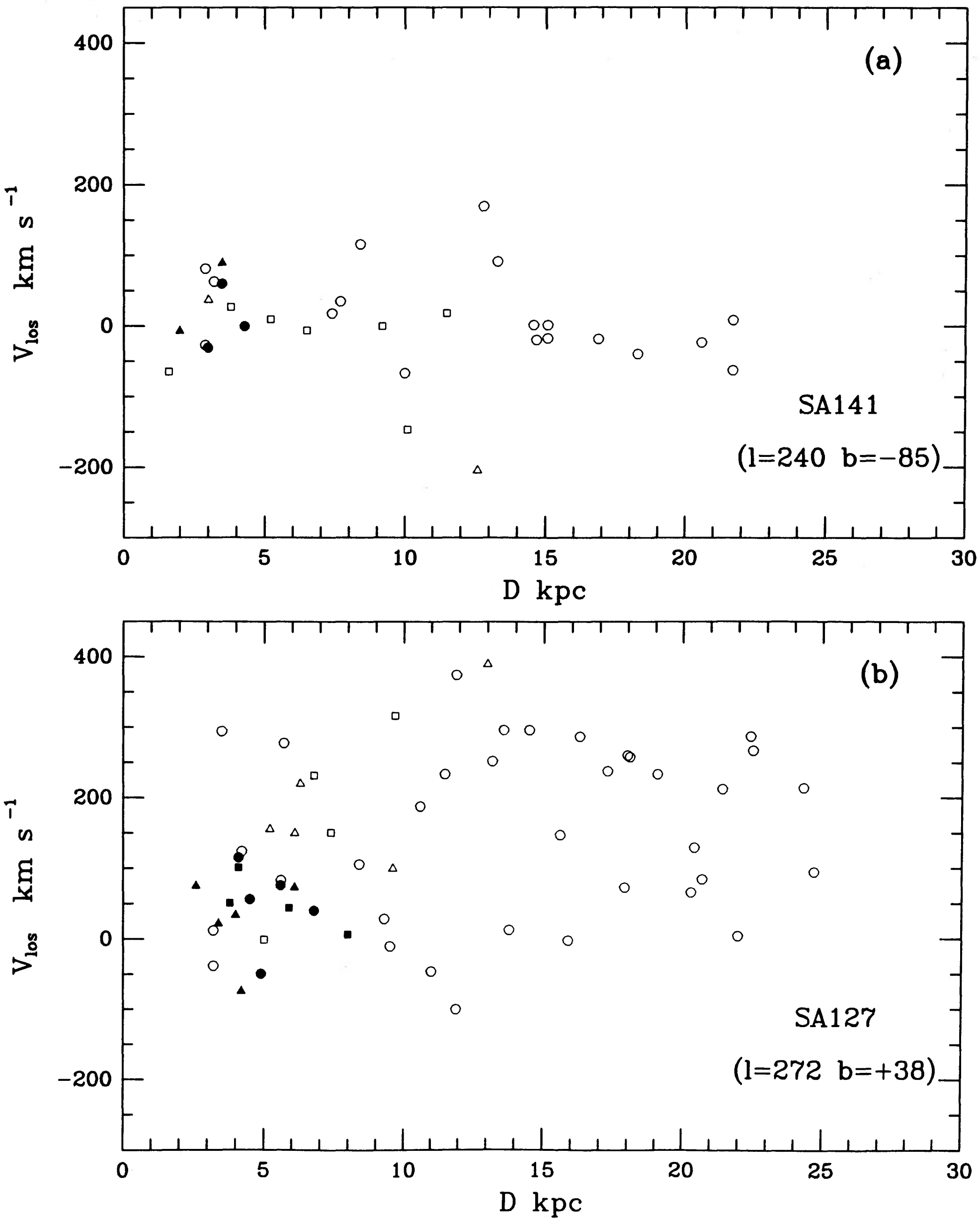

FIG. 15.—Kinematics with distance for the halo giants in SA 141 and SA 127. Symbols as in Fig. 14.

our results, we limit both these samples to $|b| > 80°$ to ensure that only the z-component of the motion is included. Table 2 suggests that the velocity dispersion of the metal-weak component rises with z and then decreases: at intermediate distances, $\sigma_{los} = 107 \pm 25$ km s^{-1} and at larger distances $\sigma_{los} = 42 \pm 10$ km s^{-1}. However, the number of stars is small, and this result depends on how the sample is partitioned. We will return to this subject later.

For the SA 127 field, the mean velocity of the metal weak stars is 153 ± 19 km s^{-1}, which is consistent with a slowly rotating stellar population observed in this direction ($l = 270°$, $b = 38°$), assuming that the circular velocity of the LSR is 220 km s^{-1}. As for SA 141, there is a suggestion from Table 2 (and Fig. 15*b*) that the velocity dispersion may increase at intermediate distances and then decrease at larger distances; again, there are not many stars, and this is only a 2 σ effect. However, it does seem clear from Figure 15 and Table 2 that the mean velocity dispersion of the metal-weak component is significantly lower towards the SGP (74 ± 10 km s^{-1}) than in the direction of SA 127 (122 ± 13 km s^{-1}), as pointed out by RF1.

Now we consider the kinematics of the more metal strong giants. These stars, with [Fe/H] > -0.7, lie between about 2 and 5 kpc from the Galactic plane. In the SA 127 field, their mean velocity is only 36 ± 14 km s^{-1} and their line-of-sight velocity dispersion is 51 ± 10 km s^{-1}. Towards the SGP, their velocity dispersion is 47 ± 16 km s^{-1}. These stars clearly belong to a rotationally supported disklike population; the data for the more metal strong giants in SA 189 (see Table 2) support this conclusion. We will discuss this population further in the next section.

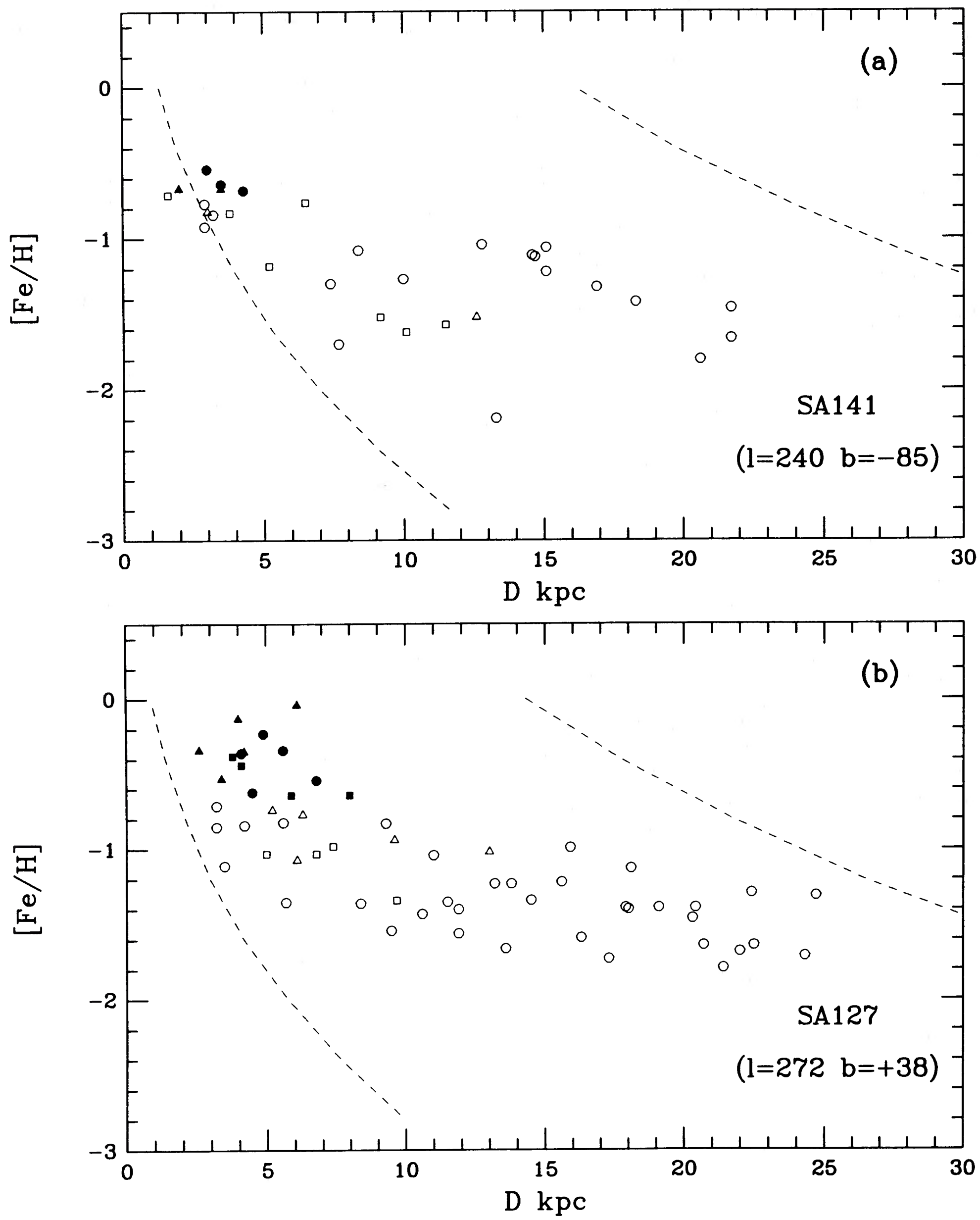

FIG. 16.—Abundance with distance from the Sun for the giants in SA 141 and SA 127. The metal stronger giants are found between 2 and 5 kpc above the plane of the disk. The metal-weak halo giants show no abundance gradient beyond a distance of about 10 kpc from the Sun. The dashed curves show the effective survey limits in this plane (see text).

V. DISCUSSION

In this section, the circular velocity at the Sun is assumed to be 220 km s^{-1}, and the galactocentric distance of the Sun is taken to be 8.5 kpc.

a) The Velocity Dispersion toward the SGP

From the data presented by RF1, it appeared that the velocity dispersion for the halo giants remained approximately constant with height up to about 25 kpc from the Galactic plane. This velocity dispersion was about 60 km s^{-1}, which was much less than the value of 124 km s^{-1} measured for the giants in the SA 127 field. Following the revision of the abundance system, there is now some evidence as shown in Table 2 that the line-of-sight velocity dispersion toward the SGP rises out to about 10 kpc and then decreases. However, this variation is not well determined, because the sample of giants is small.

We have therefore added in Figure 17 the velocity-distance data for other distant halo stars within 10° of the SGP. Our stars are shown as filled symbols. The open symbols are BHB stars from Pier (1983) and Sommer-Larsen and Christensen (1986), using Sommer-Larsen and Christensen's calibration to assign distances to Pier's stars. Figure 17 suggests that the velocity dispersion does not change much with height. To illustrate this more clearly, Figure 18 shows mean velocity dispersion points for various samples of halo stars toward the SGP, as a function of their mean distance above the plane. Identifications for the samples are given in the figure caption. The data from our SA 141 survey and from Sommer-Larsen and Christensen (1986) have each been binned into two distance intervals

TABLE 2

MEAN KINEMATICS

Subsample	Giants	⟨D⟩ (kpc)	⟨z⟩ (kpc)	⟨R⟩ (kpc)	⟨M_V⟩ (mag)	⟨[Fe/H]⟩ (dex)	⟨V_{los}⟩ (km s^{-1})	σ_{los} (km s^{-1})
				SA 141 (240.0 − 85.0)				
TD	5	3.3	3.2	8.8	1.2	−0.6	14 ± 23	47 ± 16
SA	27	10.8	10.7	14.1	−0.2	−1.3	−9 ± 15	74 ± 10
SN	7	3.2	3.2	8.8	1.3	−0.9	10 ± 20	48 ± 13
SI	10	9.6	9.6	12.8	−0.5	−1.3	−15 ± 36	107 ± 25
SF	10	17.2	17.1	19.2	−1.0	−1.4	−17 ± 14	42 ± 10
				SA 189 (277.0 − 50.0)				
TD	9	4.9	3.7	9.4	1.3	−0.4	43 ± 17	47 ± 11
SA	7	15.4	11.8	17.0	−0.8	−1.4	104 ± 38	94 ± 26
				SA 127 (270.0 + 38.6)				
TD	14	4.9	3.1	9.3	1.2	−0.4	36 ± 14	51 ± 10
SA	44	13.0	8.1	15.5	−0.5	−1.3	153 ± 19	122 ± 13
SN	13	5.4	3.4	9.7	0.9	−1.0	131 ± 29	100 ± 20
SI	17	12.4	7.7	14.6	−0.6	−1.3	157 ± 38	153 ± 27
SF	14	20.6	12.8	21.9	−1.5	−1.5	168 ± 25	90 ± 17

to reduce the uncertainty. We have also included estimates of σ_z from analysis of several samples of nearby spheroid stars.

Because of the small available number of halo stars at large z, the appearance of Figure 18 is somewhat sensitive to the way in which the data are binned (e.g., see Table 2). However, it appears at this stage that a constant velocity dispersion of about 75 km s^{-1} is consistent with the observations up to a height of about 25 kpc above the plane. (This value of 75 km s^{-1} is somewhat higher than the value of 60 km s^{-1} given by RF1.) Figure 18 also shows the expected variation of velocity dispersion with distance, assuming that the components of the velocity dispersion remain constant first in a spherical coordinate system and then in cylindrical coordinates (see RF1). For this purpose, we have adopted the values of the velocity dispersion for the halo population in the solar neighborhood derived by Bahcall and Casertano (1986): i.e., (140, 100, 76) km s^{-1}. A constant velocity dispersion with these values in cylindrical coordinates is consistent with the SGP data. We emphasize

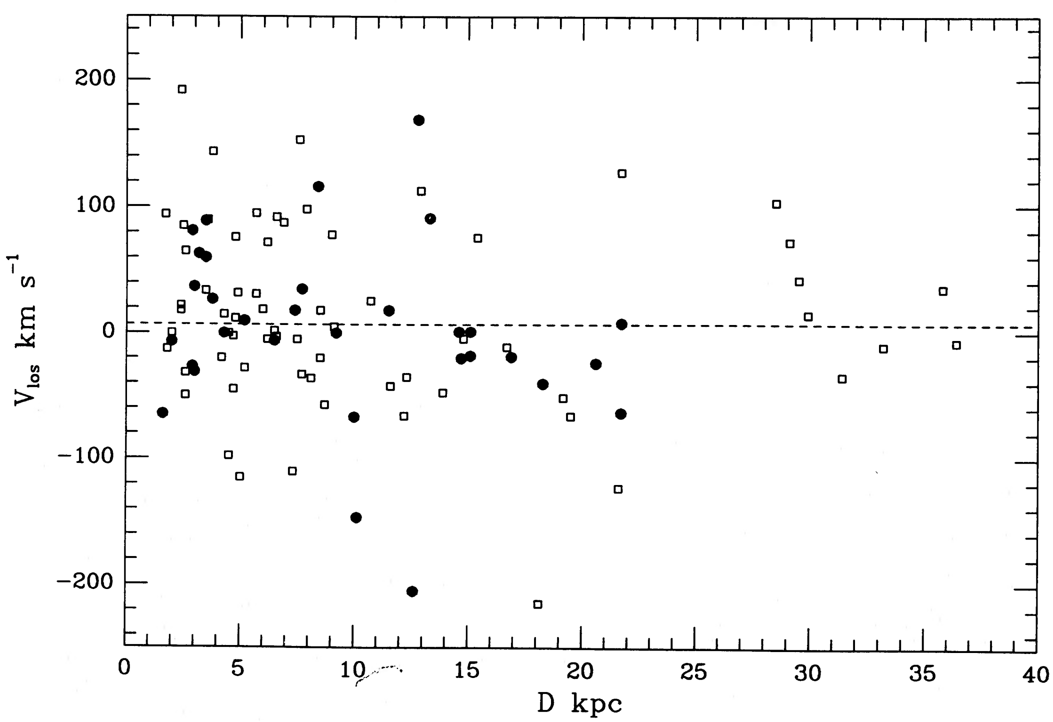

FIG. 17.—Velocity against distance for halo stars within 10° of the SGP. Filled symbols are our giants. Open squares are BHB stars from Pier (1983) and Sommer-Larsen and Christensen (1986). The broken line is at $V_{los} = 7$ km s^{-1}.

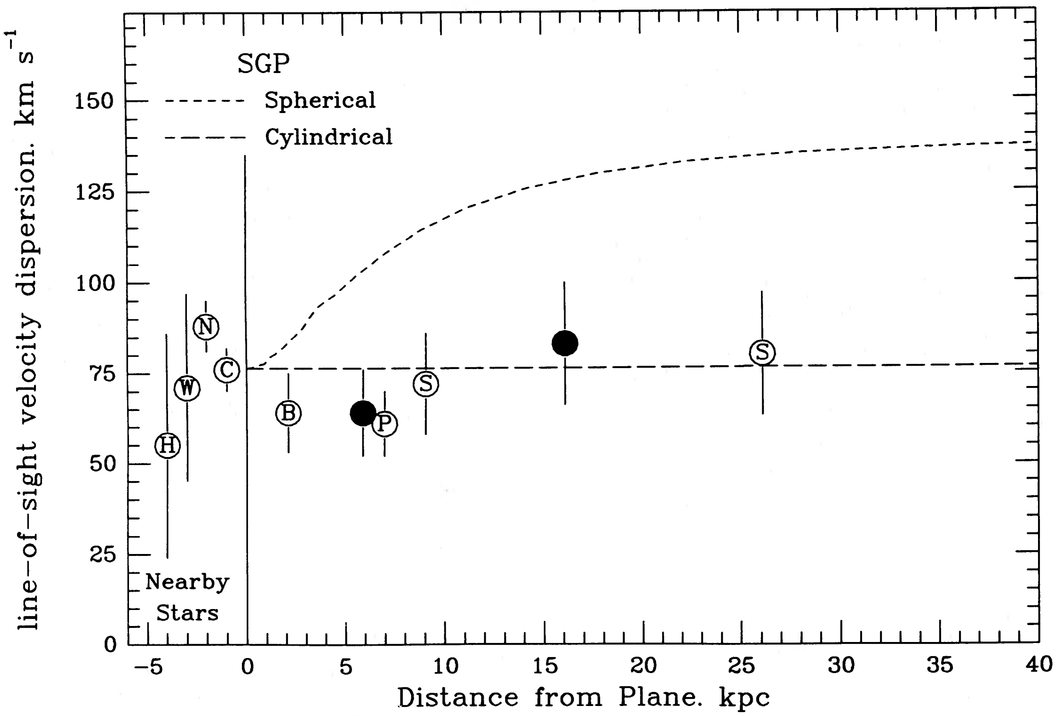

FIG. 18.—A compilation of currently available velocity dispersions toward the SGP as a function of mean distance above the plane. Solid circles show our SA 141 data binned into two distance intervals. The open circles identified by the letter within them are for metal weak giants from Beers *et al.* (1985) (B), and BHB stars from Pier (1983) (P) and Sommer-Larsen and Christensen (1986) (S). Solutions for σ_z from analysis of spheroid stars in the solar neighborhood are from Hartwick (1983) (H), Woolley (1978) (W), Norris (1986) (N), and Bahcall and Casertano (1986) (C). We also show the expected velocity dispersions for the two cases where the dispersions are assumed constant in a spherical and in a cylindrical coordinate system.

that this is only a convenient description of the data and is in no way unique; however, a constant velocity dispersion in spherical coordinates is inconsistent with the observations.

In his study of a large sample of nearby non–kinematically selected metal weak stars, Norris (1986) found a value for σ_z of 85 ± 4 km s^{-1}, as shown in Figure 18. However, he noted that the 48 objects within 10° of the Galactic poles and more than 4 kpc from the galactic plane have a σ_z value of only 64 ± 7 km s^{-1}. Norris suggests that the difference between his global and polar values of σ_z could result from small-scale clumping in velocity space. (We note again the similar velocities and abundances for our four halo giants at a distance of about 15 kpc in SA 141 [see Fig. 15*a*].)

Several authors have constructed dynamical models to investigate the dynamical implications of the low velocity dispersion observed toward the SGP. White (1985) and Levison and Richstone (1986) made scale-free models in a logarithmic spherical potential: their models require a flattened distribution of halo stars (axial ratio ≤ 0.4) to reproduce the observed kinematics. On the other hand, the observed distribution of halo objects suggests that the halo is nearly spherical: see Freeman (1987) for a review of this problem. Sommer-Larsen (1987) showed that some of the kinematical properties of the halo could be fitted by less flattened models, with axial ratio ≈ 0.8, for models which are not scale-free and in which the outermost stars are in predominantly circular orbits. However, his models were not able to reproduce the strong anisotropy observed in the kinematics of the K giants. Dejonghe and de Zeeuw (1988) constructed a halo model in a Stäckel potential that is a good approximation to the potential of the Galactic model of Bahcall, Schmidt, and Soneira (1982). They assumed that the halo stars are distributed on thin tube orbits (i.e., shell orbits). Their model can therefore reproduce the low velocity dispersion observed at high Galactic latitude but is not so successful for the lower latitude fields. However, future extensions of this approach, including orbits of nonzero radial action, appear promising. We conclude at this stage that the apparently near-spherical shape of the Galactic halo has not yet been reconciled with the existing velocity dispersion data.

b) The Metal-strong Giants

Figure 14*b* suggests that there is a fairly sharp break in the kinematics of the giants, at an abundance of [Fe/H] ≈ -0.7. The metal weaker stars belong to the slowly rotating halo, while the metal stronger stars are part of a rapidly rotating disklike population. A similar transition is seen for stars in the solar neighborhood (e.g., Norris, Bessell, and Pickles 1985). However, in SA 127 these stars are between 2 and 5 kpc above the Galactic plane. They are therefore not members of the classical old disk, which has a scale height of about 300–350 pc (e.g., Pritchet 1983). A few stars in this abundance range appear in our SGP field, all again within 5 kpc of the plane; their velocity dispersion is 47 ± 16 km s^{-1}. The catalog of 418 G and K giants at the Galactic poles, by Hartkopf and Yoss (1982) and Yoss, Neese, and Hartkopf (1987), contains only a few stars in precisely the range of height and abundance represented by our metal stronger stars in SA 127. However, above 1.5 kpc from the plane, there are 35 relatively metal strong giants ([Fe/H] > -0.8) in this catalog; their vertical velocity dispersion is 37 ± 4 km s^{-1}.

In their abundance and vertical kinematics, these giants are intermediate between the thin disk ($\sigma_z \approx 20$ to 25 km s^{-1}) and the metal-weak, halo ($\sigma_z \approx 75$ km s^{-1}). Although our survey is in no sense complete, it does appear from Figure 15 that a significant proportion of the giants in the $z = 2$–5 kpc range have [Fe/H] > -0.7. From their kinematics and location in the Galaxy, these stars are obviously part of a disklike population, close to rotational equilibrium.

The typical velocity dispersion components and asymmetric drift for these intermediate abundance stars can be estimated from the data in SA 127. The observed line-of-sight velocity dispersion is 51 ± 10 km s^{-1} and their mean velocity is 36 ± 14 km s^{-1}. We make the following assumptions: (1) the vertical velocity dispersion of these stars is 37 ± 4 km s^{-1}, by analogy with the Yoss, Neese, and Hartkopf stars toward the Galactic poles at similar heights above the plane; (2) the ratio of the radial to the azimuthal velocity dispersion components $\sigma_R/\sigma_\phi = \sqrt{2}$, consistent with a flat rotation curve and as observed for the thin disk; (3) the circular velocity at the mean galactocentric distance of 9.3 kpc for these stars is 220 km s^{-1}; (4) the off-diagonal terms of the velocity dispersion are zero in cylindrical (R, ϕ, z) coordinates. With these assumptions, the intermediate abundance stars in SA 127 have $\sigma_R = 77 \pm 16$ km s^{-1} and their asymmetric drift is 29 ± 19 km s^{-1}.

We can compare these adopted values for the velocity dispersion components $(\sigma_R, \sigma_\phi, \sigma_z) = (77 \pm 16, 54 \pm 11, 34 \pm 4)$ km s^{-1} and the asymmetric drift of 29 ± 19 km s^{-1} with those derived by others for stars that probably belong to the same population. Very recently, Friel (1988) presented velocities for giants in her Serpens field at ($l = 36°$, $b = 51°$). Her sample includes 32 stars with [Fe/H] > -0.8 at a mean height of 1.3 kpc above the plane. Their mean line-of-sight velocity is -29 ± 9 km s^{-1} and their velocity dispersion is 50 ± 6 km s^{-1}. From this relatively large velocity dispersion, she argues that these stars are not members of the old thin disk. If her stars belong to the same population as our intermediate abundance giants, with the same velocity dispersion components and asymmetric drift as those adopted above, then the expected mean line-of-sight velocity for the Serpens stars is -18 ± 8 km s^{-1} and the expected velocity dispersion is 54 ± 9 km s^{-1}. These expected values are well within the errors of Friel's observed values. Strömgren (1987) gives velocity dispersions for nearby F and early G stars as a function of their abundance. His most metal weak group, with $-0.70 \geq$ [Fe/H] ≥ -0.79, has velocity dispersion components $(65 \pm 9, 54 \pm 8, 38 \pm 6)$ km s^{-1}, and the asymmetric drift is 22 ± 11 km s^{-1}. This sample of nearby stars with intermediate abundance and our more distant sample clearly have very similar kinematics.

We can use the observed kinematics of this population of intermediate-abundance stars to put some limits on its radial scale length. We further assume that it has an exponential radial density distribution with scale length h, that its rotation and velocity dispersion are independent of height above the plane and that its scale height and anisotropy are independent of radius. Because the asymmetric drift is much smaller than the circular velocity, it follows that the asymmetric drift $= (\sigma_R{}^2/2 \times 220)(2R/h - 0.5)$, where R is the radius and the velocities are in km s^{-1} (see van der Kruit and Freeman 1986). The velocity dispersion and asymmetric drift of this intermediate abundance population are then consistent, within the errors, for any plausible radial scale length larger than about 4.5 kpc. For comparison, the Galactic thin disk has a scale length that is probably between 4 and 5 kpc (see Freeman 1987). The vertical structure of the intermediate population, and its relation to star count data near the poles, is discussed by Sandage (1987). He shows that a value of $\sigma_z = 42$ km s^{-1} is consistent with a vertical scale height of 940 pc for a realistic vertical force law.

The interpretation of these intermediate abundance stars depends on the working picture of the Galaxy. One view is that (beyond a few kpc from the Galactic center) there are three major galactic components: the thin disk, the thick disk, and the metal-weak halo (e.g., Wyse and Gilmore 1988; Freeman 1987). We would then identify the intermediate-abundance stars with the thick disk; they are too far from the plane to belong to the thin disk, and their abundances and rotation are obviously not appropriate for the metal-weak halo. With this identification, the thick disk is a rapidly rotating population, intermediate in its abundance and vertical kinematics but rotating almost as rapidly as the thin disk at the same radius.

An alternative view (Norris 1987) is that the component usually identified as the thick disk is merely the higher energy, slightly metal weaker tail of the thin disk. He points out that the asymmetric drift, for a sample of nearby G and K giants with [Fe/H] ≈ -0.6 and $\sigma_z \approx 35$ km s^{-1}, is no larger than about 30 km s^{-1}. These stars appear to be the nearby counterparts of our intermediate abundance stars at higher z, and our data are therefore consistent with his view. Sandage and Fouts (1987) found a similar asymmetric drift and a similar value of σ_z for the intermediate-abundance stars that they identified as thick disk members from their catalog of nearby high proper motion stars. Also, the similarity of the ratio σ_R/σ_z for the old thin disk (40 km s^{-1}/23 km s^{-1}) and for this intermediate population (77 km s^{-1}/37 km s^{-1}) is striking, and may suggest that similar heating processes have acted on both. This does not, however, resolve the question of whether the thin and thick disks are discrete components. This issue, which has been reviewed at length by Freeman (1987), is important because of its implications about the formation and evolution of the Galactic disk and the possible occurrence of discrete events such as satellite accretion. Whatever the answer to this difficult question, one fact has become clear. The intermediate population is intermediate only in its abundance and velocity dispersion: its rotation is similar to that of the old thin disk itself.

We gratefully acknowledge discussions with John Bahcall, Herwig Dejonghe, Gerard Gilmore, David Hartwick, John Norris, Allan Sandage, Martin Schwarzschild, Jesper Sommer-Larsen, Rosemary Wyse, and Tim de Zeeuw. We are particularly grateful to Martin Schwarzschild for his continued encouragement. We thank Chris Flynn and Heather Morrison for making some observations for us, and the Anglo Australian Observatory for support during the spectroscopic observations. This work was completed while we were visiting the Institute for Advanced Study, Princeton.

APPENDIX

DISTANCE ESTIMATION

Absolute magnitudes M_V for the giants were determined from the observed $(B-V)_0$ color and estimated metal abundance [Fe/H] to M_V, using an empirical calibration. This calibration was evaluated using the observed cluster giant branches at different metal abundance. The adopted metal abundance, distance modulus, and reddening of the six clusters used to set up the calibration

TABLE 3

ADOPTED CLUSTER PARAMETERS

Calibration Cluster	⟨[Fe/H]⟩ (dex)	$(m - M)_V$ (mag)	$E(B-V)$ (mag)
M92	−2.24	14.43	0.01
M3	−1.66	14.79	0.01
M13	−1.65	14.06	0.02
M5	−1.40	14.29	0.03
47 Tuc	−0.71	13.12	0.04
M67	−0.00	9.56	0.06

are listed in Table 3. The age dependence of this calibration is assumed to be small compared with other uncertainties; the field K giants are assumed to be of similar age to the clusters of similar metal abundance.

The empirical calibration is defined by a fourth-order polynomial and a shift in $(B-V)_0$ and M_V which are linear in [Fe/H]:

$$M_V = A_0 + 1.11[\mathrm{Fe/H}] + 0.443 ,$$

where

$$A_0 = 68.08 - 170.3C + 163.4C^2 - 71.20C^3 + 11.75C^4$$

and

$$C = \min \{[(B - V)_0 - 0.10[\mathrm{Fe/H}] - 0.013], 1.80\} . \tag{A1}$$

The grid over the color-magnitude range is shown in Figure 19. Distance errors were estimated using a Monte Carlo procedure. The error estimates used for this calculation are as follows: $(B-V)$, ± 0.02 mag; V, ± 0.03 mag; $E(B-V)$, ± 0.01 mag; [Fe/H], ± 0.15 for AAT and ± 0.3 for the PCA data. The resulting rms distance errors are shown as a function of distance in Figure 20*a* using the same symbols as in Figure 14. The fractional rms distance errors are shown as a function of $(B-V)_0$ in Figure 20*b*.

Although some authors state that the K giant branch is very steep and therefore photometric distance estimates are dangerous (e.g., Wyse and Gilmore 1988), Figure 19 shows that the K giant branch is in fact rather flat for $(B-V)_0 > 1.0$. The photometric distances are therefore good to about 10%–20%, if the abundances of the stars are known to an accuracy of about 0.15 to 0.3 dex, as shown in Figure 20.

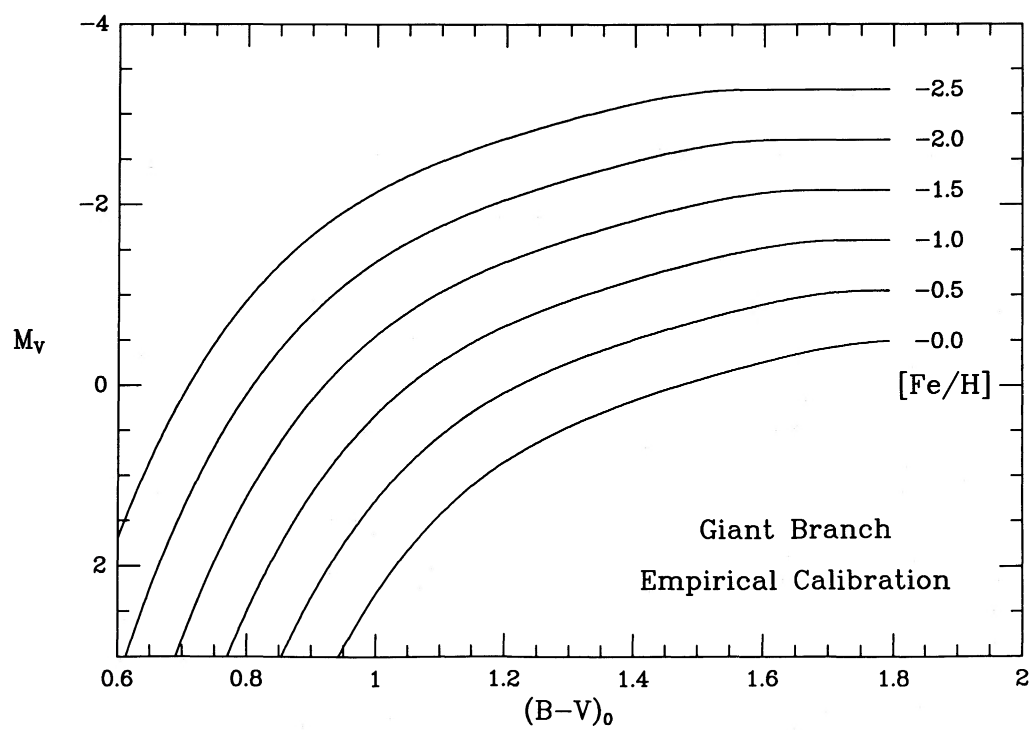

FIG. 19.—The empirical calibration grid of the giant branch defined by a fourth-order polynomial and a shift in $(B-V)_0$ and M_V which are linear in [Fe/H]

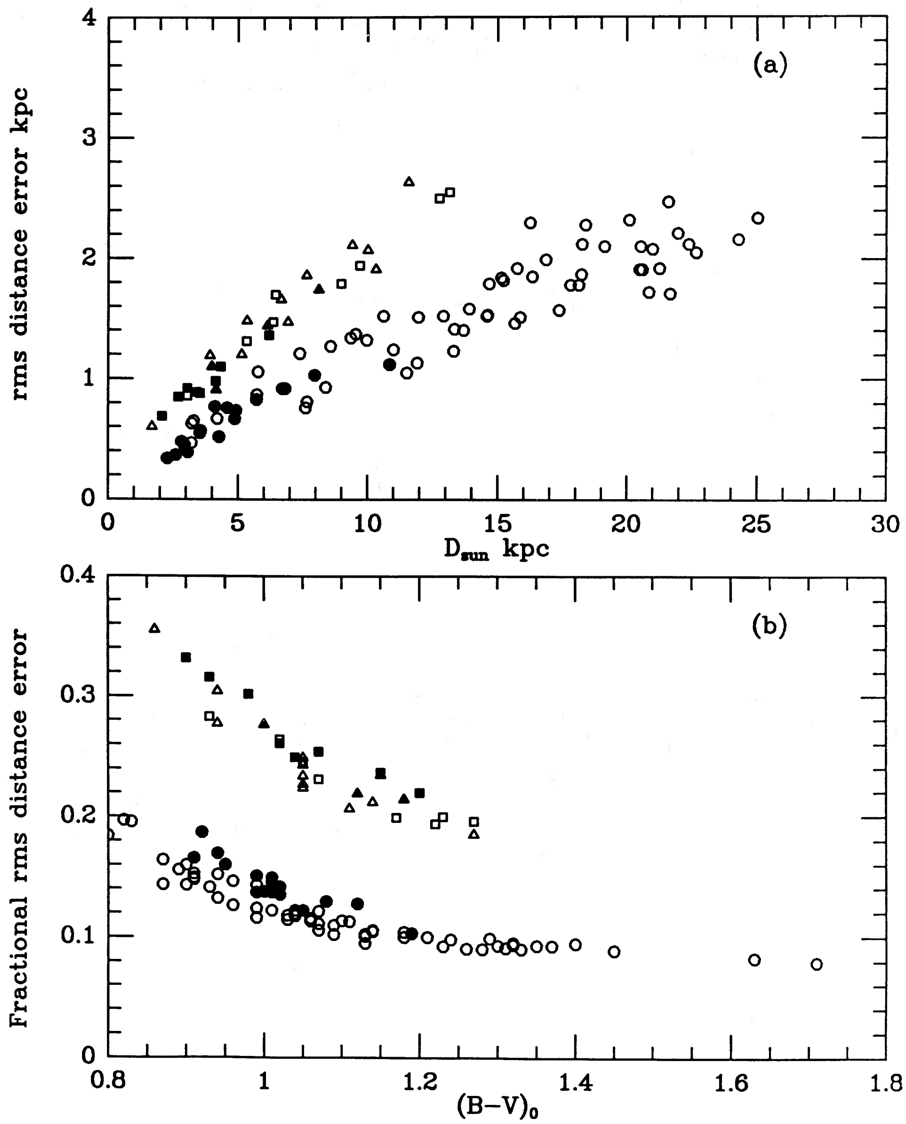

FIG. 20.—(*a*) Estimated rms error in distance as a function of distance from Sun. (*b*) Fractional distance error as a function of $(B-V)_0$. Symbols same as in Fig. 14.

REFERENCES

Bahcall, J. N., and Casertano, S. 1986, *Ap. J.*, **308**, 347.
Bahcall, J. N., Schmidt, M., and Soneira, R. M., 1982, *Ap. J.* (*Letters*), **258**, L23.
Beers, T. C., Preston, G. W., and Shectman, S. A. 1985, *A.J.*, **90**, 2089.
Dejonghe, H., and de Zeeuw, T. 1988, *Ap. J.*, **329**, 720.
Friel, E. 1987, *A.J.*, **93**, 1388.
———. 1988, *A.J.*, **95**, 1727.
Freeman, K. C. 1987, *Ann. Rev. Astr. Ap.*, **25**, 603.
Hartkopf, W., and Yoss, K. 1982, *A.J.*, **87**, 1679.
Hartwick, F. D. A. 1983, *Mem. Soc. Astr. Italiana*, **54**, 51.
Levison, H. F., and Richstone, D. O. 1986, *Ap. J.*, **308**, 627.
Morgan, W. W., Keenan, P. C., and Kellman, E. 1943, *MKK Yerkes Atlas* (Chicago: University of Chicago Press).
Norris, J. E. 1986, *Ap. J. Suppl.*, **61**, 667.
———. 1987, *Ap. J.* (*Letters*), **314**, L39.
Norris, J. E., Bessell, M. S., and Pickles, A. J. 1985, *Ap. J. Suppl.*, **58**, 463.
Pier, J. R. 1983, *Ap. J. Suppl.*, **53**, 791.
Pritchet, C. 1983, *A.J.*, **88**, 1476.
Ratnatunga, K. U. 1983, Ph.D. thesis, The Australian National University.
Ratnatunga, K. U., and Freeman, K. C. 1983, in *IAU Colloquium 78, Astronomy with Schmidt-like Telescopes*, ed. M. Capaccioli (Dordrecht: Reidel), p. 261.
———. 1985, *Ap. J.*, **291**, 260 (RF1).
Sandage, A. 1987, *A.J.*, **93**, 610.
Sandage, A., and Fouts, G. 1987, *A.J.*, **93**, 74.
Sommer-Larsen, J. 1987, *M.N.R.A.S.*, **227**, 25P.
Sommer-Larsen, J., and Christensen, P. R. 1986, *M.N.R.A.S.*, **219**, 837.
Strömgren, B. 1987, in *The Galaxy*, ed. G. Gilmore and R. Carswell (Dordrecht: Reidel), p. 229.
Suntzeff, N. B. 1980, *A.J.*, **85**, 408.
Tonry, J., and Davis, M. 1979, *A.J.*, **84**, 1511.
van der Kruit, P. C., and Freeman, K. C. 1986, *Ap. J.*, **303**, 556.
White, S. D. M. 1985, *Ap. J.* (*Letters*), **294**, L99.
Woolley, R. 1978, *M.N.R.A.S.*, **184**, 311.
Wyse, R., and Gilmore, G. 1988, *A.J.*, **95**, 1404.
Yoss, K., Neese, C., and Hartkopf, W. 1987, *A.J.*, **94**, 1600.
Zinn, R. 1985, *Ap. J.*, **293**, 424.

K. C. FREEMAN: Mount Stromlo and Siding Spring Observatories, Private Bag, Woden, P.O. ACT 2606, Australia

KAVAN U. RATNATUNGA: NASA/Goddard Space Flight Center, Greenbelt, MD 20771